

## Spectrogoniometry and modeling of martian and lunar analog samples and Apollo soils

Jeffrey R. Johnson<sup>a,\*</sup>, Michael K. Shepard<sup>b</sup>, William M. Grundy<sup>c</sup>, David A. Paige<sup>d</sup>, Emily J. Foote<sup>d</sup>

<sup>a</sup> Johns Hopkins University Applied Physics Laboratory, 11101 Johns Hopkins Road, 200-W230, Laurel, MD 20723-6005, United States

<sup>b</sup> Bloomsburg University, 400 East Second St., Bloomsburg, PA 89557, United States

<sup>c</sup> Lowell Observatory, 1400 West Mars Hill Rd., Flagstaff, AZ 86001, United States

<sup>d</sup> University of California, Los Angeles, 595 Charles Young Drive East, Box 951567, Los Angeles, CA 90095-1567, United States

### ARTICLE INFO

#### Article history:

Received 17 May 2012

Revised 19 November 2012

Accepted 4 December 2012

Available online 19 December 2012

#### Keywords:

Spectrophotometry

Regoliths

Mars, Surface

Moon, Surface

Radiative transfer

### ABSTRACT

We present new visible/near-infrared multispectral reflectance measurements of seven lunar soil simulants, two Apollo soils, and eight martian analog samples as functions of illumination and emission angles using the Bloomsburg University Goniometer. By modeling these data with Hapke theory, we provide constraints on photometric parameters (single scattering albedo, phase function parameters, macroscopic roughness, and opposition effect parameters) to provide additional “ground truth” photometric properties to assist analyses of spacecraft data. A wide range of modeled photometric properties were variably related to albedo, color, grain size, and surface texture. Finer-grained samples here have high single-scattering albedo values compared to their coarser-grained counterparts, as well as lower macroscopic roughness values. The Mars analog samples and Apollo soils exhibit slightly lower opposition effect width parameter values than the lunar analogs, whereas the opposition effect magnitude is not well constrained by the models. The Mars analog soils are typically relatively backscattering and consistent with fairly rough particles with a moderate density of internal scatterers, similar to the in situ observations of some soils by the Mars Exploration Rover (MER) Spirit. Some lunar analog soil models result in moderately-forward scattering behaviors, as do the two Apollo soils. Other fine-grained and/or glass-rich lunar analog samples populate a narrowly forward-scattering regime similar to model results from observations of some rover tracks observed by the MER Opportunity rover and some dust-poor “gray” rocks by the Spirit rover. An experiment to mimic the spherule-rich soils observed by Opportunity demonstrated a large decrease in single-scattering albedo compared to spherule-free soil surfaces, as well as increased surface roughness, narrow opposition effects, and a significant increase in backscattering, similar to some of the Opportunity soils. Phase reddening effects are documented in many soils as an increase in near-infrared/visible ratios with phase angle. Some samples exhibit falloffs in these ratio phase curves at phase angles beyond 50–80° that are likely related to an increased importance of surface scattering at high phase angles. None of the lunar analog soils perfectly match the modeled photometric parameters of the two Apollo soils. The phase reddening nature of the mare soil included an upturn in ratio values at phase angles <10° that was not observed for the highland sample. It remains to be verified whether this is a consistent observation between mare and highland samples.

© 2012 Elsevier Inc. All rights reserved.

### 1. Introduction

The visible and near-infrared reflectance of planetary surfaces is influenced greatly by the viewing geometry and solar illumination angle. The photometric scattering properties of materials can vary substantially as a result of differences in the porosity, composition, grain size and internal heterogeneity of the constituent particles,

as well as surface roughness at scales ranging from microns to meters. Surface and orbital observations acquired at a variety of emission, solar incidence, and phase angles provide the data necessary to model the surface bidirectional reflectance distribution function (BRDF). The most commonly used models are the formulations of Hapke (1993, 2012) that attempt to approximate the scattering behavior of closely packed particles based on radiative transfer theory. Such models can be used to normalize reflectance data from spacecraft images to common illumination geometries, thus allowing more direct comparison of images obtained at different times of day. When combined with laboratory measurements, these models can also assist interpretations of compositional and mineralogical

\* Corresponding author. Fax: +1 240 228 8939.

E-mail addresses: [Jeffrey.R.Johnson@jhuapl.edu](mailto:Jeffrey.R.Johnson@jhuapl.edu) (J.R. Johnson), [mshpard@bloomu.edu](mailto:mshpard@bloomu.edu) (M.K. Shepard), [grundy@lowell.edu](mailto:grundy@lowell.edu) (W.M. Grundy), [dap@mars.ucla.edu](mailto:dap@mars.ucla.edu) (D.A. Paige), [efoote@ucla.edu](mailto:efoote@ucla.edu) (E.J. Foote).

information from spectral reflectance observations. While such models can provide useful constraints on the single scattering albedo and relative degree of forward versus backward scattering of surfaces, recent laboratory tests reduce confidence in the ability of Hapke theory to reliably constrain the microphysical interpretations of surfaces from these parameters (Helfenstein and Shepard, 2011; Shepard and Helfenstein, 2007, 2011). Nonetheless, ongoing spectrogoniometric measurements and Hapke modeling of planetary analogs can provide observations useful for inter-comparisons of the photometric scattering properties of planetary surfaces, particularly when applied to spacecraft observations.

We have acquired visible/near-infrared multispectral reflectance measurements of lunar soil simulants and martian analog samples as functions of illumination and emission angles using the Bloomsburg University Goniometer (BUG) laboratory (Shepard, 2001). By modeling these data with Hapke theory, we provide constraints on photometric parameters (single scattering albedo, phase function parameters, macroscopic roughness, and opposition effect parameters) to provide additional “ground truth” photometric properties relevant to analyses of spacecraft data. For example, photometric studies of the Moon have used observations by Clementine (e.g., Buratti et al., 1996; Blewett et al., 1997), the SMART-1 AMIE camera (e.g., Shevchenko et al., 2003), the Kaguya Spectral Profiler (Yokota et al., 2011), the Lunar Reconnaissance Orbiter (Kaydash et al., 2010; Shkuratov et al., 2011; Hapke et al., 2012), and ground-based observing programs (e.g., Kieffer and Stone, 2005). For Mercury, photometric analyses using the Mercury Dual Imaging System (MDIS) instrument on the MESSENGER spacecraft were completed by Domingue et al. (2010, 2011a,b). Photometric studies have been conducted for Mars using ground-based and spacecraft data from Mariner through the Mars Exploration Rovers and Mars Reconnaissance Orbiter (e.g., Arvidson et al., 1989a,b; Guinness et al., 1997; Pinet et al., 2005; Johnson et al., 2006a,b, 2008; Jehl et al., 2008; Shaw et al., 2012).

Previous efforts to acquire and model analog samples have contributed to our appreciation of the variety of photometric properties exhibited by minerals, rocks, and soils of planetary interest. Mustard and Pieters (1989) used an early version of Hapke's model to analyze the BRDFs of mineral mixtures and found that silicates are more forward scattering than hematite, although particle roughness and albedo strongly influenced the scattering properties. Capaccioni et al. (1990) studied the broadband (400–800 nm) reflectance of different grain sizes of diabase, peridotite, quartz sand, and meteorite samples at phase angles 2–50° and suggested that the shape of phase curves (change in reflectance with phase angle) varied with composition as well as grain size and packing. Kamei and Nakamura (2002) studied olivine and meteorite sample BRDFs acquired from 2° to 155° (at one incidence angle) and suggested that smaller particle size samples were more forward-scattering. Cord et al. (2003) presented data and Hapke model results for fresh and altered basalts at various grain sizes, and demonstrated variability in modeled parameters with wavelength. However, their data were acquired only over phase angles from 20° to 115°, which did not fully constrain the opposition effect (increased brightness near zero phase). Conversely, Kaasalainen (2003) and Näränen et al. (2004) acquired data from 0° to 25° phase angles over fresh and oxidized basalts at various grain sizes and packing states. They noted increases in the reflectance and opposition peak at lower surface roughness and for compacted samples. Hapke et al. (1993) measured eight Apollo lunar soils at 442 nm and 633 nm at phase angles 1–70° to demonstrate the invariance of opposition peak widths with wavelength.

Piatek et al. (2004) modeled data acquired at 633 nm from ~0° to 140° of calcium carbonate, aluminum, and ferric oxide powders. The latter exhibited an extremely wide opposition surge (~40°). However, they found little correlation between particle size and the modeled scattering parameters, and called into question model

assumptions that particles be treated as fundamental light-scattering units even when closely spaced. They concluded that further laboratory studies were needed to understand the scattering properties of closely packed, rough-surface, irregular particles. Shepard and Helfenstein (2007) expanded on that work by modeling a collection of different sands, oxide powders, and clays to test Hapke theory, but did not emphasize planetary analog samples. They also reported changes in sample single scattering albedo with compaction, a weak correlation between the opposition surge width and the macroscopic roughness parameter, but little correlation between estimated sample porosity and opposition effect parameters. They concluded that the model parameters were not necessarily intrinsic to the individual particles comprising a given sample, but a combination of packing, roughness, and other particulate properties. Hapke et al. (2009) reached similar conclusions in a study using observations of small (<26 μm) glass spheres.

Shkuratov et al. (2007) presented lab measurements of powdered and compressed olivine, feldspar, volcanic ash, loess, and clay at two wavelengths (440 nm, 630 nm) from 2° to 150° phase angle. They reported no wavelength variation with opposition effect width. Gunderson et al. (2006) presented goniometric measurements in the principal plane (2–85° phase angles) for the lunar soil simulant JSC-1 (McKay et al., 1994) at 564 nm and ~950 nm, and reported strong correlations between some Hapke model parameters. Gunderson and Thomas (2008) acquired data at ~1000 nm of the JSC-1, JSC-1AF, and MLS lunar simulants, and the JSC Mars-1 simulant, and provided qualitative descriptions of their phase curves and opposition effects. Souchon et al. (2011) acquired data at five wavelengths (559–960 nm) at 25–130° phase angles for volcanic sands and rocks at grain sizes of 45–2000 μm. They reported strongly forward-scattering behaviors for large, glassy samples and/or translucent monocrystals. Beck et al. (2012) acquired data of powdered meteorites (including lunar meteorite MAC 88105) at five wavelengths from 450 to 900 nm over phase angles 3–150°. Although they reported no clear differences between meteorite groups, their data demonstrated pronounced spectral reddening with phase angle (“phase reddening”), a phenomenon observed in nearly all planetary bodies. Similar work was done by Kawakami and Nakamura (2007), who studied the opposition surge at 1064 nm of carbonaceous chondrite meteorites at various grain sizes and compaction states over 0–30° phase angles.

Despite uncertainties associated with the microphysical interpretation of the Hapke parameters used to describe the opposition effect, it is apparent from these recent works that the model is still useful as a means of parameterizing and comparing model results among spectrogoniometric data sets such as those presented here. Our approach concentrated on acquiring data for a variety of planetary analogs using at least five wavelengths (415–950 nm), and to model the results using Hapke formulations that incorporate a parameter uncertainty estimation method to provide quantitative estimates of the degree to which photometric parameters are constrained by the data sets. We also investigated the wavelength dependency of modeled parameters and considered potential correlations with scattering properties (cf. Cord et al., 2003).

## 2. Materials and methods

### 2.1. Lunar analog samples

We analyzed seven lunar analog soil materials to provide a range of mineralogy, composition, and physical properties comparable to lunar (and to some extent asteroidal and mercurian) soils. These included the Minnesota Lunar Simulant MLS-1 sieved to <1 mm and 500–840 μm size fractions, as well as a plasma-processed, glass-rich

simulant created from MLS-1 (Weiblen and Gordon, 1988); the historic JSC-1 lunar simulant sieved to <1 mm (McKay et al., 1994; Allen et al., 1994); a new JSC-1 lunar simulant sieved to <1 mm (JSC-1A) and to an average grain size of 24  $\mu\text{m}$  (JSC-1AF) from Orbitec Technologies Corp (NASA-MSFC, 2006); and the FJS-1 simulant from Shimizu Corp., Japan sieved to a median grain size of 70  $\mu\text{m}$  (Kanamori et al., 1998). The Minnesota Lunar Simulant MLS-1 is a high-titanium crystalline basalt with a median grain size of  $\sim 100 \mu\text{m}$  and a chemical composition that approximates Apollo 11 soil, albeit without glass or agglutinates (Colwell et al., 2007; Goldich, 1970; Weiblen et al., 1990). JSC-1 is a glass-rich ( $\sim 50\%$ ) basaltic ash with a median grain size of  $\sim 70 \mu\text{m}$ , a composition more similar to Apollo 14 and 15 soils, and geotechnical properties more appropriate to lunar soil (McKay et al., 1994; Clark et al., 2004). The JSC-1A simulant matches the composition and particle size

distribution of the original JSC-1, having also originated from the Merriam Crater volcanic cinder cone in Arizona (NASA\_MFSC, 2006). FJS-1 is Mt. Fuji basalt prepared to a median grain size of 70  $\mu\text{m}$ , with a composition similar to Apollo 14 samples (Kanamori et al., 1998). This range of lunar simulants was selected to provide a suitable suite of analogs to describe the scattering properties relevant to lunar-like terrains.

Two Apollo soil samples were also analyzed to provide mare and highland samples for comparison to the analog soils (cf. Foote et al., 2009, 2012). This included the Apollo 11 mature mare soil 10084 (splits 161, 2010, 2011) and the Apollo 16 mature highland soil 68810.2. For these measurements the standard BUG geometric coverage was supplemented by constructing an elongated sample holder for measurements in and perpendicular to the principal plane (Foote et al., 2009). These measurements allowed expanded

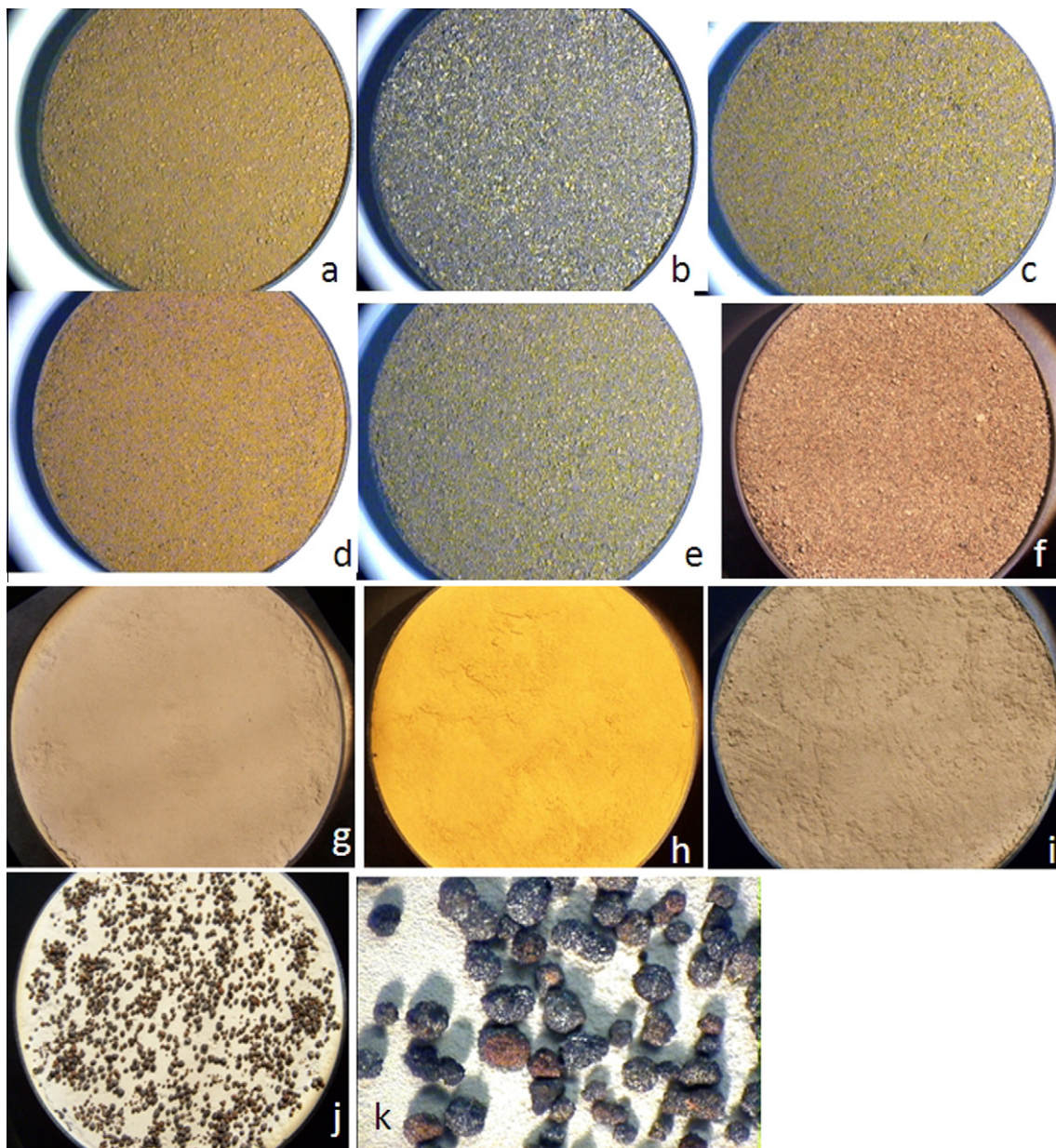


**Fig. 1.** Digital photographs of Mars analog soils. Sample cup is 6 cm diameter. Colors are not normalized between images. (a) HWMK 904 (AREF 236); (b) HWMK 940 (AREF 237); (c) JSC-1 < 1 mm; (d) HWMK 101 (AREF 235) < 50  $\mu\text{m}$ ; (e) HWMK 600 (AREF 238) 50–1000  $\mu\text{m}$ ; (f) HWMK 600 (150–1000  $\mu\text{m}$ ); (g) SCB5; (h) Pahala ash; (i) JSC-1 < 45  $\mu\text{m}$ ; (j) SCB5 with spherules; (k) photographic close-up of spherules; field of view is  $\sim 1 \text{ cm}$ . (For interpretation of the references to color in this figure legend, the reader is referred to the web version of this article.)

geometric coverage to incidence angles of 0–75° and phase angles of 3–155°, comprising a total of 769 measurements per wavelength.

## 2.2. Martian analog samples

Eight martian analogs soils that can be loosely grouped as “palagonitic soils” were analyzed to provide a range of endmember compositions. Palagonites describe a large class of poorly-crystalline, variably weathered basaltic glasses with visible/near-infrared spectral properties analogous to those observed for Mars (e.g., Bell, 1996; Bell et al., 2000; Schiffman et al., 2002; Drief and Schiffman, 2004; Seiferlin et al., 2008). The samples analyzed here included four Hawaiian soils from Mauna Kea (Morris et al., 2000, 2001; Hamilton et al., 2008) and the JSC-1 Mars analog simulant (Allen et al., 1998), all sieved to <1 mm grain size. The Mauna Kea samples comprise palagonitic tephra HWMK 101 (also designated as sample AREF 235) and HWMK 600 (AREF 238), a sample with natrojarosite (HWMK 940, AREF 237), and a sample with smectite (HWMK 904, AREF 236). A 150–1000  $\mu\text{m}$  size fraction from the HWMK 600 sample was used as well. Also included were palagonitic soil collected from South Point on the island of Hawaii (Pahala ash) sieved to <53  $\mu\text{m}$ , and a separate split of JSC-1 sieved to <45  $\mu\text{m}$  used in previous work (cf. Johnson et al., 2002). We also included a hematite–siderite spherule-bearing paleosol (e.g., White et al., 2000, 2001) as an analog to the spherule-bearing sulfate sedimentary rocks observed at the Mars Exploration Rover (MER) Meridiani Planum landing site. The sample is from the middle Cretaceous Dakota Formation in the Sioux City Brick Pit (SCBP, Sioux City, Iowa). These samples contain siderite spherules <2–3 mm in diameter with thin hematite rims, whereas the silt/sandstone matrix material is much finer-grained. The spherules were extracted

and cleaned from the paleosol to perform the following experiment: After acquiring data of the powdered matrix soil (<45  $\mu\text{m}$ ; Fig. 1g), we gently sprinkled the extracted spherules on top of the matrix-only sample (Fig. 1j) to examine the photometric effects of small spherules on a fine-grained substrate as observed extensively by the MER Opportunity rover. During emplacement some spherules were slightly embedded in the soil matrix (Fig. 1k).

## 2.3. Data acquisition

Multispectral measurements of the samples were acquired using the Bloomsburg University Goniometer (BUG). This instrument is capable of measuring the full BRDF of a sample using several broadband interference filters (50 nm FWHM) from 400 to 1000 nm at incidence angles of 0–60°, emission angles of 0–80°, and phase angles of 3° to ~145°, typically providing 680 measurements per filter. All measurements were calibrated using the reflectance standard Spectralon™ illuminated normally, such that the data were reduced to radiance factor (Hapke, 1993, 2012), with relative uncertainties <2%. Full details of the instrument and data acquisition methods are provided in Shepard and Helfenstein (2007, 2011). We acquired measurements of the samples as described above using at least five filters. For the JSC-1 (bulk) Mars sample and the HWMK 101, 904, 940, and 600 samples (AREF 235–238), data were acquired at 430, 450, 480, 530, 600, 670, 750, 800, 860, 900, 930, 990 nm. For the remaining Mars analog soils (and the two Apollo soils) filters were used at 450, 550, 750, and 950 nm. For the lunar analogs, we used filters at 410, 550, 750, and 950 nm. For each sample the surface was leveled with a straight edge to provide as smooth a surface as possible, followed by a small tap to settle the particles. As shown in Figs. 1 and 2,

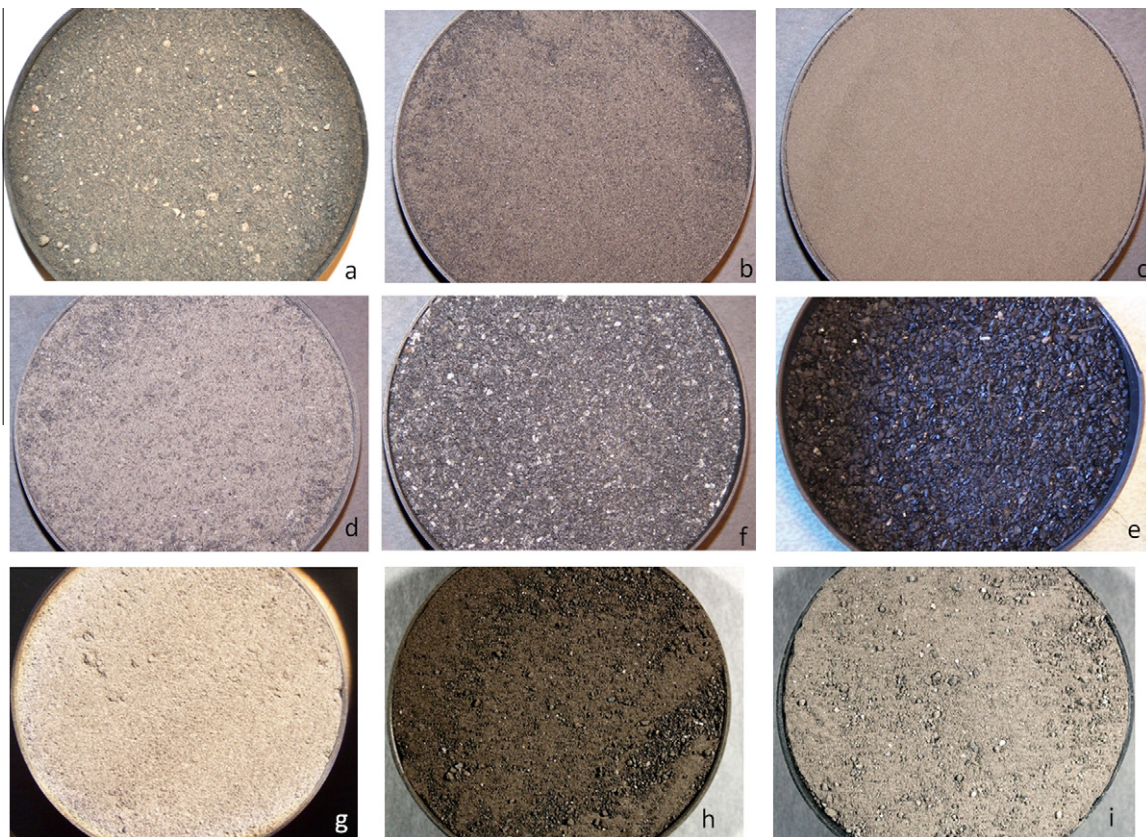


**Fig. 2.** Digital photographs of lunar analog samples and Apollo 11 and 16 soils. Sample cup is 6 cm diameter. Colors are not normalized between images. (a) JSC-1; (b) JSC-1A; (c) JSC-1AF; (d) MLS1-bulk; (e) MLS1 540–800  $\mu\text{m}$ ; (f) MLS1-glass; (g) FJS-1; (h) Apollo sample 10084; (i) Apollo sample 68810.

some fine-grained samples tended to exhibit residual clumping at the scale of millimeters.

### 3. Hapke theory

#### 3.1. Hapke modeling

The Hapke model is frequently used to analyze the photometric properties of planetary surfaces (Hapke, 1993, 2012). It has the advantage of being computationally inexpensive, allowing inversion by iterative numerical methods (e.g., Marquardt, 1963; Nelder and Mead, 1965), while providing constraints on scattering parameters if sufficient phase angle coverage is available. For each data set acquired for a given wavelength, we ran models using 1-term and 2-term Henyey–Greenstein (HG) phase functions, using an isotropic multiple scattering approximation (IMSA model) and the Hapke (1993) version of the analytic approximation of the isotropic scattering H function. We acknowledge that if some of the particles studied here single-scatter light anisotropically (e.g., narrow forward-scattering lobes), then the assumption of isotropically-scattering grains may be insufficient. However, such effects are likely of greatest significance for particles with very high albedo, unlike the particles of interest in this study.

Output from the isotropic 1-term HG phase function models included the single scattering albedo ( $w$ ), the macroscopic roughness  $\bar{\theta}$ , the phase function asymmetry parameter ( $\xi$ ), and the opposition effect width ( $h$ ) and magnitude ( $B_0$ ). In theory, the  $B_0$  is physically related to the opacity of particles, where a value of 1.0 implies that all light is scattered at the surface and the particle is opaque (e.g., Domingue et al., 1997). As such, we limit the maximum value of  $B_0$  in our models to 1.0. The parameter  $h$  was considered physically related to porosity and particle size distribution by Hapke (1993) such that less porous materials (or those with lower ratios of largest-to-smallest particle size, depending on the assumed particle size power law distribution) have large values of  $h$  (cf. Helfenstein and Veverka, 1987; Hapke, 1993). However, recent studies such as Hapke (2008) and Shepard and Helfenstein (2011) have cast doubt on the physical interpretations of the  $h$  and  $B_0$  parameters. The form of the 1-term HG phase functions as a function of phase angle ( $g$ ) used here is:

$$P(g) = \frac{(1 - \xi^2)}{[1 + 2\xi \cos(g) + \xi^2]^{3/2}}$$

The 2-term HG function models provided the asymmetry parameter ( $b$ ) and forward scattering fraction ( $c'$ ). The form of the 2-term HG phase function we use here is:

$$P(g) = \frac{c'(1 - b^2)}{[1 + 2b \cos(g) + b^2]^{3/2}} + \frac{(1 - c')(1 - b^2)}{[1 - 2b \cos(g) + b^2]^{3/2}}$$

We note that other workers define the 2-term HG function differently such that their  $c$  parameter represents the backward scattering fraction (e.g., Hartmann and Domingue, 1998; Cord et al., 2003). To be consistent with those studies and our previous photometric studies of Mars (Johnson et al., 2006a,b,c, 2008), we convert our forward fraction parameter  $c'$  to a backward fraction  $c$  via  $c = (1 - c')$ . We also note that a different version of the 2-term HG function was used by Hapke (1993, Eq. 6.18a; 2012, Eq. 67a) and McGuire and Hapke (1995) in which their “ $c$ ” parameter is related to  $c$  by the relation “ $c$ ” =  $(2c - 1)$ .

Updated formulations of Hapke theory provide additional parameters to separate the effects of shadow-hiding and coherent backscatter on the opposition effect (Hapke, 2002, 2008, 2012; Hapke et al., 1998) and to describe the effects of sample porosity. The lack of phase angle coverage below  $\sim 3^\circ$  in the BUG datasets prevented detailed analyses of the coherent backscatter versus

shadow hiding components of the opposition effect (e.g., Nelson et al., 1998; Piatek et al., 2004). We experimented with using the updated version of the Hapke model for these data, but the inclusion of additional parameters resulted in overall model results that were not as well constrained as using the Hapke (1993) model. This may result from the non-orthogonality of the parameters, i.e., two parameters that attempt to model the same effect can offset each other and result in poor constraints on both (e.g., Goguen et al., 2010).

Under the assumption that coherent backscatter could result in values of  $B_0 > 1$  at longer wavelengths (thereby altering the shape of the opposition effect curve), we experimented with HG2 phase function model runs for all wavelengths of the AREF 235 soil (HWMK 101) without constraining the  $B_0$  parameter. Although no significant changes were observed for the  $w$ ,  $\bar{\theta}$ ,  $b$ , or  $c$  values, the  $B_0$  parameter migrated to values between 1 and 7, but with very large errors (up to 90). In addition the  $h$  parameter values correspondingly decreased by factors of 2–5 and were under-constrained for 5 of the 11 wavelengths. This demonstrated that limiting  $B_0 \leq 1.0$  resulted in better constrained model results.

#### 3.2. Parameter uncertainties

All models reported a reduced chi-square ( $\chi^2_\nu$ ) estimate of their goodness of fit. However, as is often noted by photometry researchers interaction between Hapke parameters sometimes results in non-unique solutions, especially when data are only available at limited illumination or observation geometries. In this situation, the number of fitted parameters must be reduced, if all remaining fitted parameters are to be meaningfully constrained by the data. To help monitor our ability to constrain fitted parameters, we followed the method described in Johnson et al. (2006a) to estimate one-sigma confidence limits on each of our fitted parameters, assuming an average 4% error in bidirectional reflectance. For each parameter, the value was fixed at a series of values stepping away from its best-fit value. With the parameter in question set at each of these fixed values, the other parameters were re-fitted, allowing the model to compensate for the deviation of the parameter in question from its best-fit value. These new fits resulted in a series of chi-squared values, such that for a well-constrained parameter the chi-squared values exhibit a clear minimum at the best fit parameter value and rise steeply away from that minimum. For a poorly constrained parameter, the rise away from the best fit value is more gradual, and for a completely unconstrained parameter, the slice through chi-squared space is flat. The one-sigma confidence contour coincides with the contour in chi-squared space located at the minimum chi-squared value plus one (Press, 1992), as long as the errors in the photometry data obey a Gaussian distribution with a known scale. Often, the rise in chi-squared is steeper in one direction than in the other, resulting in asymmetric confidence limits around the best-fit parameter value. This type of error indicates mainly how well the model parameters fit the available data. As such, they do not account for how missing photometric geometry coverage (i.e.,  $g < 3^\circ$  or  $g > 155^\circ$ ) could affect the results. These errors are parenthetically listed in the tables below; when parameters are under-constrained (e.g., the  $B_0$  parameter), they are indicated by “(+--, ---)” in place of uncertainty estimates.

## 4. Results

#### 4.1. BUG phase curves

Figs. 3 and 4 plot radiance factor phase curves for all analog soils at two representative wavelengths. Scatter within the overall

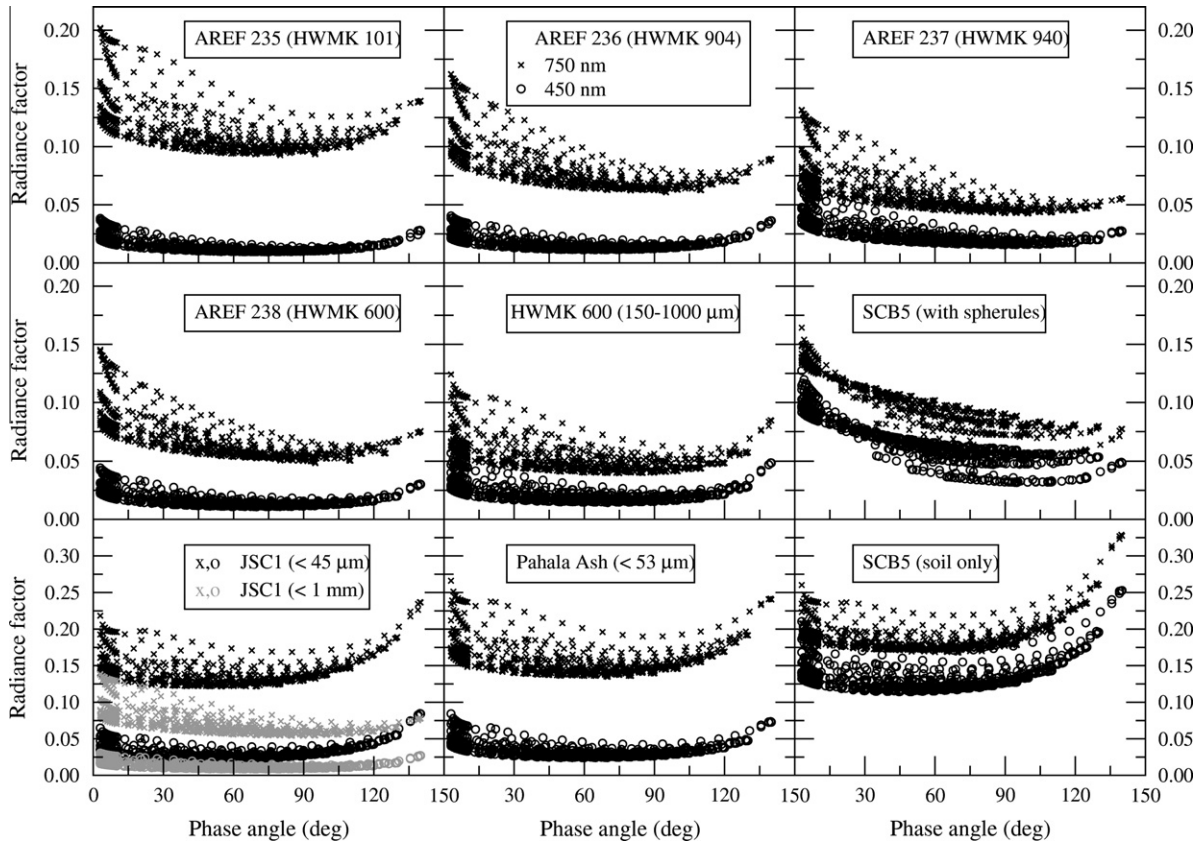


Fig. 3. Phase curves of Mars analog soils at 450 nm (circles) and 750 nm (x's).

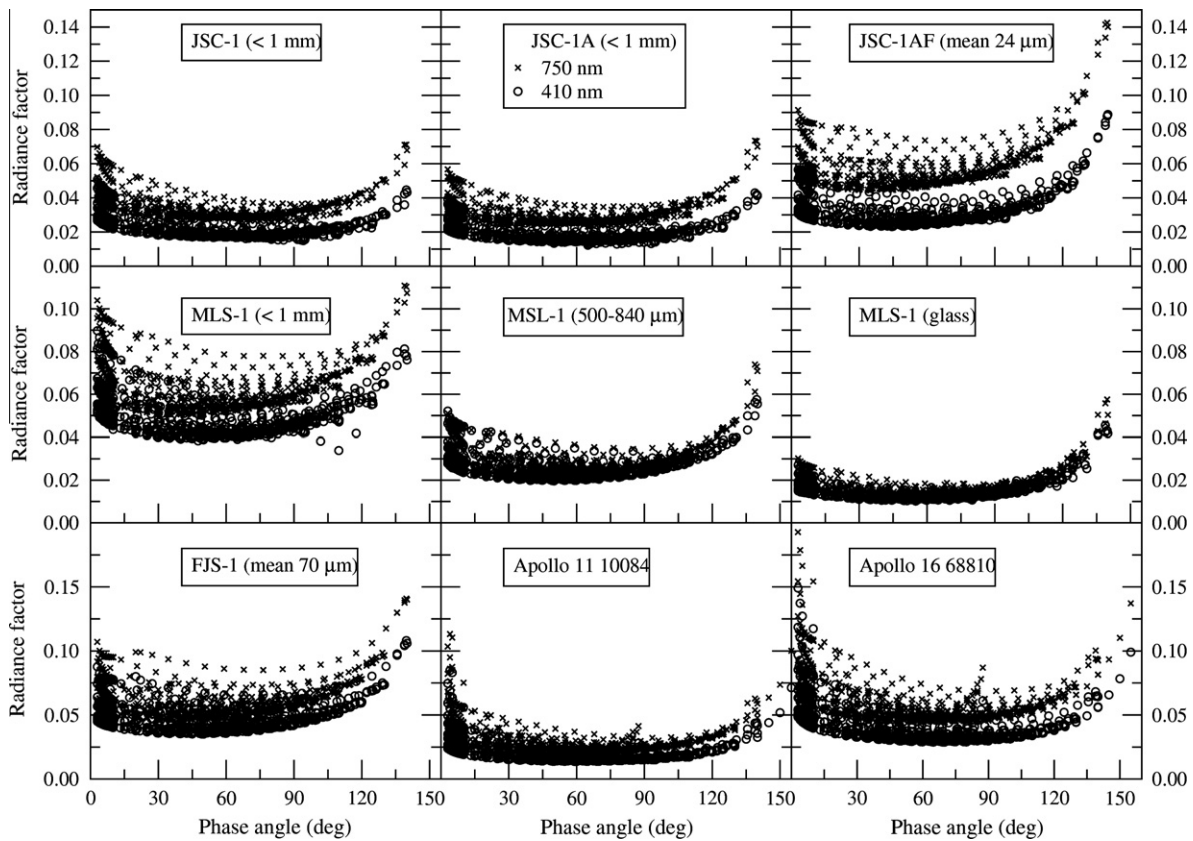


Fig. 4. Phase curves of lunar analog and Apollo soils (x's represent 750 nm observations; circles represent 410 nm for analogs and 450 nm for Apollo soils).

trends results from the variety of incidence, emission, and azimuth angles provided by a given BUG run (cf., Shepard and Helfenstein, 2011). Variations in the phase curve slopes at  $<30^\circ$  and  $>100^\circ$  demonstrate the general magnitude and symmetry of backscattering and forward scattering, respectively. Of particular interest in Fig. 3 is the change in the phase curves of the SCB5 soil from forward-scattering to backscattering upon placement of the spherules. Finer grain sizes also tend to exhibit greater forward scattering as can be observed by comparing the two grain sizes of the Mars analog JSC1 in Fig. 3 or the JSC-1A and JSC-1AF lunar analog soils in Fig. 4. Also noteworthy in Fig. 4 are the pronounced opposition surges of the two Apollo soils (cf. Foote et al., 2009, 2012) compared to the other lunar analog soils.

#### 4.2. Hapke model results

Tables 1 and 2 summarize the results for the 1-term and 2-term HG model runs for all samples. As described in Section 3.2, errors are included for each parameter. Overall  $\chi^2_v$  values demonstrate that the 2-term HG function models tend to better describe the data. Parameters under-constrained by the model are also noted. This most often this occurs for the  $B_0$  parameter, although the roughness parameter  $\bar{\theta}$  is sometimes under-constrained as well, particularly for the 1-term HG function models. The opposition effect width  $h$  is under-constrained by the 2-term HG models for some of the lunar analog soils, particularly the MLS-1 samples.

Figs. 5 and 6 show single-scattering albedo values as a function of wavelength from the 2-term HG function models. All the Mars analog soil samples (Fig. 5) exhibit albedo spectra with increasing slopes from the visible to the near-infrared, typical of palagonitic materials. The Mauna Kea samples have sufficient spectral sampling to reveal near-infrared spectral features related to ferric-bearing minerals. For comparison the lunar analogs and soils have less red and often relatively flat spectral slopes, particularly the MLS-1 and FJS-1 soils (Fig. 6). Predictably, the addition of dark, red spherules to the SCB5 soil lowers the albedo and imparts a steeper red slope in the spectrum. Finer grain sizes also show higher albedo values, as does the Apollo 16 highland sample relative to the Apollo 11 mare sample.

Spectral variability of the macroscopic roughness ( $\bar{\theta}$ ) parameters from the 2-term HG models is shown in Fig. 7. Results from 1-term HG were typically less well constrained (Tables 1 and 2). Values for most samples vary between  $13^\circ$  and  $22^\circ$ , although the fine-grained samples (SCB5, Pahala ash, JSC-1 ( $<45 \mu\text{m}$ ), and FJS-1) have the lowest  $\bar{\theta}$  values. The SCB5 soil with spherules was modeled with the highest  $\bar{\theta}$  value, as expected. Little variability with wavelength is observed for most samples, except for Pahala ash, FJS-1, MLS-1 (500–840  $\mu\text{m}$ ) and MLS-1 (bulk) samples, which exhibit moderate ( $>5^\circ$ ) decreases with increasing wavelength.

Opposition effect width ( $h$ ) parameter values modeled from 1-term HG functions are plotted versus wavelength in Fig. 8. Results from 2-term HG models were more often less well constrained (Tables 1 and 2). Typical  $h$  values for Mars analog soils were  $\sim 0.06$ – $0.07$ , with little variability with wavelength. The finest grained samples exhibited slightly elevated  $h$  values (e.g., Pahala ash, JSC-1 ( $<45 \mu\text{m}$ )), with the largest values modeled for the SCB5 soil ( $h \sim 0.09$ ). The introduction of spherules to SCB5 reduced these values to the lowest observed for all samples ( $h \sim 0.02$ – $0.04$ ), and introduced a slight decrease in  $h$  with increasing wavelength. The lunar analogs were modeled with slightly greater  $h$  values ( $h \sim 0.07$ – $0.10$ ), although the two Apollo soils exhibited the lowest values ( $h \sim 0.05$ – $0.07$ ). None exhibited appreciable trends with wavelength. Fig. 9 plots the asymmetry parameter ( $\xi$ ) for all samples from 1-term HG function models as a function of wavelength. The fine-grained samples tend to be forward scattering ( $\xi > 0$ ), with the exception of slight negative  $\xi$  values modeled for Pahala

ash samples. The low albedo MLS samples are also modeled as forward scattering (regardless of grain size). The SCB5 sample changes from forward to backscattering upon inclusion of the spherules, as suggested by the phase curves in Fig. 3. Most samples exhibit nearly constant or increasing  $\xi$  values with wavelength, suggesting a more forward-scattering behavior at longer wavelengths. Conversely, the SCB5 soil with spherules is the only sample that exhibits a more backscattering behavior with increasing wavelength.

Fig. 10 presents the 2-term HG phase function parameters for the Mars analog samples compared to the values of the artificial particle types studied by McGuire and Hapke (1995). In that study, particles with different degrees of heterogeneity exhibited discrete  $b$  and  $c$  values related to deviations from a particle's internal and spherical perfection. Smooth, clear spheres plot furthest to the right (less isotropic and greater forward scattering) whereas rough particles with microcracks or inclusions plot nearer the top (greater backscattering). The AREF/HWMK Mars analog samples (Fig. 8a) tend to exhibit  $b$  and  $c$  values that exhibit characteristics consistent with particles that are relatively rough and have a moderate density of internal scatterers. Fig. 8a also plots average values modeled from Spirit MER Pancam data of representative soils in the plains of Gusev Crater and the base of Husband Hill that bracket the AREF/HWMK sample values. The JSC-1 bulk sample and the Pahala ash exhibit similar  $b$  and  $c$  values (Fig. 10b), although the JSC-1 ( $<45 \mu\text{m}$ ) and SCB5 soils are notably more forward scattering. The addition of spherules to the SCB5 soil results in a more backscattering surface, similar to the spherule-rich soils by the Opportunity MER Pancam near Vostok crater south of Endurance crater (also plotted in Fig. 10b).

The 2-term HG phase function parameters for the lunar analog and Apollo soils are shown in Fig. 11. Although the FJS-1, JSC1 (bulk), and two Apollo soil samples plot in a region similar to the agglutinate and rough/clear spheres, most of the soils exhibit low  $c$  and high  $b$  values indicative of a narrow forward-scattering peak, unlike any of the artificial particles from McGuire and Hapke (1995). The inset plot in Fig. 11 shows more clearly the cluster of values in this region. Repeated attempts to model these data sets with variable starting conditions provided similar results, as did a complete reacquisition of BUG data and modeling of the MLS-1 (500–840  $\mu\text{m}$ ) sample. We discuss this regime of scattering behavior further below.

Although most model results show little variability in the  $b$  and  $c$  parameters with wavelength, several exceptions occur. As shown in Figs. 12 and 13, the SCB5 soil with spherules and JSC-1 ( $<45 \mu\text{m}$ ) soil exhibit outlier points in at 950 nm and 550 nm, respectively. The JSC lunar analogs all exhibit spectral variability, whereas the FJS-1 and MLS samples were more consistent, and the Apollo soils cluster better than any analog sample. The only consistent trends with wavelength were increasing  $b$  values exhibited by the SCB5 soils (more so for the spherule-laden sample) and the bulk JSC-1 and MLS-1 lunar analogs (which showed an increase in  $b$  values, indicating a narrowing of the scattering lobes). These samples also exhibited decreasing  $c$  values (greater forward scattering) with wavelength (although very minor for the bulk MLS-1 sample). The Apollo 68810 soil also exhibited this trend. However, we note that these trends may be a consequence of sampling only four wavelengths for these soils. One could interpret increases in  $c$  values with wavelength for the AREF 235 (HWMK 101) and AREF 238 (HWMK 600) samples if only four similar wavelengths were used. These spectral variations are discussed further below.

#### 4.3. Phase reddening

We also investigated “phase reddening” (the brightening of a surface at longer wavelengths with increasing phase angle) by observing the degree to which near-infrared/visible radiance factor

**Table 1**  
Hapke model results for Mars analog soils.

Sample	$w$	$\bar{\theta}$ (°)	$h$	$B0$	$\xi$	$b$	$c$	$\chi^2_{\nu}$	No.
<i>AREF 235 (HWMK 101)</i>									
450 nm	0.15	10	0.063	1.00	−0.154			0.01	680
(HG1)	+0.00, −0.00	+1, −1	+0.002, −0.003	+−, −−	+0.005, −0.005				
(HG2)	0.22	19	0.041	1.00		0.376	0.286	0	680
	+0.00, −0.00	+0, −0	+0.002, −0.001	+−, −−		+0.002, −0.003	+0.005, −0.005		
480 nm	0.26	11	0.063	1.00	−0.115			0.03	680
(HG1)	+0.00, −0.00	+1, −0	+0.010, −0.002	+−, −−	+0.010, −0.004				
(HG2)	0.37	22	0.032	1.00		0.39	0.225	0.01	680
	+0.00, −0.01	+0, −0	+0.002, −0.001	+−, −−		+0.004, −0.004	+0.006, −0.005		
530 nm	0.4	13	0.064	1.00	−0.118			0.05	680
(HG1)	+0.00, −0.00	+1, −1	+0.005, −0.005	+−, −−	+0.005, −0.007				
(HG2)	0.51	22	0.034	1.00		0.349	0.296	0.01	680
	+0.00, −0.00	+0, −0	+0.002, −0.001	+−, −−		+0.005, −0.005	+0.008, −0.008		
600 nm	0.61	8	0.063	1.00	−0.124			0.05	680
(HG1)	+0.00, −0.00	+1, −0	+0.002, −0.005	+−, −−	+0.002, −0.005				
(HG2)	0.67	15	0.027	1.00		0.291	0.469	0.01	680
	+0.00, −0.00	+0, −0	+0.001, −0.000	+−, −−		+0.003, −0.003	+0.008, −0.005		
670 nm	0.7	16	0.053	1.00	−0.13			0.18	680
(HG1)	+0.00, −0.00	+0, −0	+0.007, −0.006	+−, −−	+0.006, −0.007				
(HG2)	0.79	21	0.01	1.00		0.372	0.36	0.1	680
	+0.01, −0.00	+0, −0	+0.002, −0.001	+−, −−		+0.005, −0.005	+0.009, −0.010		
750 nm	0.78	10	0.056	1.00	−0.111			0.12	640
(HG1)	+0.00, −0.00	+1, −0	+0.005, −0.003	+−, −−	+0.006, −0.004				
(HG2)	0.84	16	0.017	1.00		0.343	0.365	0.03	640
	+0.00, −0.00	+0, −0	+0.001, −0.000	+−, −−		+0.004, −0.004	−0.006, +0.006		
800 nm	0.76	12	0.055	1.00	−0.129			0.11	680
(HG1)	+0.00, −0.00	+0, −0	+0.004, −0.005	+−, −−	+0.005, −0.003				
(HG2)	0.83	19	0.016	1.00		0.358	0.351	0.04	680
	+0.00, −0.00	+0, −0	+0.002, −0.000	+−, −−		+0.004, −0.004	+0.006, −0.008		
860 nm	0.73	14	0.057	1.00	−0.115			0.15	640
(HG1)	+0.00, −0.00	+0, −0	+0.005, −0.005	+−, −−	+0.005, −0.006				
(HG2)	0.81	20	0.01	1.00		0.386	0.316	0.06	640
	+0.01, −0.00	+1, −0	+0.002, −0.001	+−, −−		+0.002, −0.009	+0.004, −0.011		
900 nm	0.76	2	0.047	1.00	−0.133			0.06	680
(HG1)	+0.00, −0.00	+−, −−	+0.007, −0.001	+−, −−	+0.005, −0.004				
(HG2)	0.8	13	0.028	0.93		0.256	0.555	0.05	680
	+0.00, −0.00	+0, −0	+0.007, −0.003	+−, −−		+0.005, −0.005	+0.011, −0.013		
930 nm	0.75	11	0.051	1.00	−0.12			0.07	680
(HG1)	+0.00, −0.00	+1, −0	+0.005, −0.002	+−, −−	+0.005, −0.003				
(HG2)	0.8	16	0.016	1.00		0.304	0.454	0.03	680
	+0.00, −0.00	+0, −0	+0.001, −0.000	+−, −−		+0.002, −0.003	+0.005, −0.007		
990 nm	0.74	11	0.053	1.00	−0.126			0.1	680
(HG1)	+0.00, −0.00	+0, −0	+0.005, −0.003	+−, −−	+0.005, −0.004				
(HG2)	0.81	17	0.014	1.00		0.334	0.42	0.03	680
	+0.00, −0.00	+0, −0	+0.001, −0.000	+−, −−		+0.003, −0.002	+0.006, −0.005		
<i>AREF 236 (HWMK 904)</i>									
450 nm	0.18	5	0.066	1.00	−0.104			0.02	680
(HG1)	+0.00, −0.00	+1, −2	+0.004, −0.002	+−, −−	+0.006, −0.003				
(HG2)	0.23	14	0.045	1.00		0.332	0.318	0	680
	+0.01, −0.00	+2, −0	+0.012, −0.010	+−, −−		+0.004, −0.002	+0.002, −0.027		
480 nm	0.22	14	0.058	1.00	−0.151			0.02	680
(HG1)	+0.00, −0.00	+1, −1	+0.011, −0.001	+−, −−	+0.010, −0.004				
(HG2)	0.28	20	0.068	1.00		0.326	0.335	0	680
	+0.04, −0.00	+2, −1	+0.013, −0.040	+−, −−		+0.034, −0.003	+0.036, −0.013		
530 nm	0.31	12	0.064	1.00	−0.132			0.03	680
(HG1)	+0.00, −0.00	+0, −1	+0.003, −0.002	+−, −−	+0.005, −0.004				
(HG2)	0.4	20	0.036	1.00		0.345	0.317	0.01	680
	+0.00, −0.00	+0, −0	+0.002, −0.001	+−, −−		+0.003, −0.005	+0.006, −0.007		
600 nm	0.48	7	0.059	1.00	−0.14			0.04	680
(HG1)	+0.00, −0.00	+2, −0	+0.012, −0.004	+−, −−	+0.011, −0.004				
(HG2)	0.55	15	0.041	1.00		0.288	0.457	0.01	680
	+0.00, −0.00	+0, −0	+0.002, −0.001	+−, −−		+0.003, −0.004	+0.009, −0.007		
670 nm	0.55	10	0.061	1.00	−0.145			0.06	680
(HG1)	+0.00, −0.00	+0, −0	+0.003, −0.002	+−, −−	+0.004, −0.004				
(HG2)	0.62	15	0.027	1.00		0.308	0.481	0.02	680
	+0.02, −0.01	+3, −0	+0.032, −0.008	+−, −−		+0.010, −0.019	+0.013, −0.069		
750 nm	0.63	12	0.045	1.00	−0.167			0.08	640
(HG1)	+0.02, −0.01	+4, −1	+0.058, −0.013	+−, −−	+0.049, −0.008				
(HG2)	0.72	19	0.019	1.00		0.327	0.447	0.03	640
	+0.00, −0.00	+0, −0	+0.002, −0.000	+−, −−		+0.003, −0.004	+0.007, −0.008		
800 nm	0.65	13	0.062	1.00	−0.131			0.07	680
(HG1)	+0.00, −0.00	+0, −0	+0.002, −0.004	+−, −−	+0.003, −0.005				
(HG2)	0.74	20	0.025	1.00		0.332	0.375	0.03	680
	+0.00, −0.00	+0, −0	+0.002, −0.001	+−, −−		+0.004, −0.004	+0.008, −0.009		

Table 1 (continued)

Sample	w	$\bar{\theta}$ (°)	h	B0	$\xi$	b	c	$\chi^2_{\nu}$	No.
860 nm	0.6	15	0.061	1.00	-0.132			0.09	640
(HG1)	+0.00, -0.00	+0, -0	+0.004, -0.004	+-, ---	+0.004, -0.005				
(HG2)	0.69	20	0.017	0.99		0.349	0.384	0.04	640
	+0.00, -0.00	+0, -0	+0.002, -0.000	+-, ---		+0.005, -0.005	+0.009, -0.009		
900 nm	0.66	6	0.055	1.00	-0.11			0.06	680
(HG1)	+0.00, -0.00	+1, -1	+0.012, -0.001	+-, ---	+0.010, -0.001				
(HG2)	0.73	15	0.026	1.00		0.294	0.421	0.02	680
	+0.00, -0.00	+0, -0	+0.002, -0.001	+-, ---		+0.004, -0.004	+0.006, -0.008		
930 nm	0.67	12	0.059	1.00	-0.109			0.07	680
(HG1)	+0.00, -0.00	+0, -1	+0.009, -0.002	+-, ---	+0.005, -0.005				
(HG2)	0.74	18	0.02	1.00		0.324	0.386	0.02	680
	+0.00, -0.00	+0, -0	+0.001, -0.000	+-, ---		+0.003, -0.003	+0.006, -0.006		
990 nm	0.7	11	0.055	1.00	-0.107			0.09	680
(HG1)	+0.00, -0.00	+1, -0	+0.011, -0.002	+-, ---	+0.010, -0.003				
(HG2)	0.78	18	0.017	1.00		0.338	0.357	0.03	680
	+0.00, -0.00	+0, -0	+0.001, -0.000	+-, ---		+0.004, -0.003	+0.006, -0.006		
<i>AREF 237 (HWMK 940)</i>									
450 nm	0.24	8	0.058	1.00	-0.195			0.01	680
(HG1)	+0.00, -0.00	+1, -1	+0.001, -0.001	+-, ---	+0.002, -0.002				
(HG2)	0.27	15	0.055	1.00		0.273	0.611	0	680
	+0.03, -0.00	+6, -0	+0.013, -0.015	+-, ---		+0.007, -0.003	+0.006, -0.063		
480 nm	0.32	15	0.06	1.00	-0.182			0.01	680
(HG1)	+0.00, -0.00	+1, -0	+0.001, -0.002	+-, ---	+0.002, -0.004				
(HG2)	0.39	21	0.05	1.00		0.289	0.505	0	680
	+0.00, -0.00	+0, -0	+0.001, -0.002	+-, ---		+0.004, -0.001	+0.011, -0.005		
530 nm	0.41	17	0.058	1.00	-0.182			0.02	680
(HG1)	+0.00, -0.00	+0, -0	+0.002, -0.002	+-, ---	+0.001, -0.002				
(HG2)	0.47	22	0.04	1.00		0.285	0.555	0.01	680
	+0.00, -0.00	+1, -0	+0.008, -0.002	+-, ---		+0.003, -0.008	+0.008, -0.018		
600 nm	0.49	14	0.058	1.00	-0.173			0.02	680
(HG1)	+0.00, -0.00	+0, -0	+0.001, -0.001	+-, ---	+0.002, -0.002				
(HG2)	0.55	19	0.036	1.00		0.271	0.599	0.01	680
	+0.00, -0.01	+0, -1	+0.004, -0.000	+-, ---		+0.001, -0.008	+0.010, -0.005		
670 nm	0.5	15	0.058	1.00	-0.167			0.03	680
(HG1)	+0.00, -0.00	+0, -0	+0.001, -0.002	+-, ---	+0.002, -0.004				
(HG2)	0.56	20	0.031	1.00		0.282	0.554	0.01	680
	+0.00, -0.00	+0, -0	+0.001, -0.000	+-, ---		+0.003, -0.003	+0.008, -0.007		
750 nm	0.53	15	0.062	1.00	-0.153			0.02	640
(HG1)	+0.00, -0.00	+0, -1	+0.002, -0.011	+-, ---	+0.001, -0.010				
(HG2)	0.57	18	0.033	1.00		0.26	0.603	0.01	640
	+0.00, -0.00	+0, -0	+0.002, -0.000	+-, ---		+0.003, -0.003	+0.007, -0.010		
800 nm	0.51	14	0.054	1.00	-0.147			0.03	680
(HG1)	+0.01, -0.00	+1, -0	+0.014, -0.004	+-, ---	+0.013, -0.001				
(HG2)	0.59	21	0.031	1.00		0.3	0.429	0.01	680
	+0.00, -0.00	+0, -0	+0.001, -0.000	+-, ---		+0.005, -0.003	+0.010, -0.006		
860 nm	0.46	16	0.067	1.00	-0.155			0.04	680
(HG1)	+0.01, -0.00	+1, -0	+0.003, -0.017	+-, ---	+0.007, -0.010				
(HG2)	0.55	22	0.028	1.00		0.312	0.45	0.02	680
	+0.01, -0.00	+0, -0	+0.002, -0.001	+-, ---		+0.006, -0.004	+0.011, -0.010		
900 nm	0.46	12	0.06	1.00	-0.154			0.02	680
(HG1)	+0.00, -0.00	+0, -0	+0.001, -0.001	+-, ---	+0.002, -0.002				
(HG2)	0.52	18	0.038	1.00		0.273	0.529	0.01	680
	+0.00, -0.01	+0, -1	+0.011, -0.001	+-, ---		+0.001, -0.010	+0.005, -0.015		
930 nm	0.46	14	0.062	1.00	-0.145			0.03	680
(HG1)	+0.00, -0.01	+0, -2	+0.007, -0.011	+-, ---	+0.002, -0.010				
(HG2)	0.53	20	0.037	0.99		0.29	0.468	0.01	680
	+0.00, -0.00	+0, -0	+0.003, -0.001	+-, ---		+0.005, -0.005	+0.010, -0.012		
990 nm	0.47	12	0.062	1.00	-0.145			0.03	680
(HG1)	+0.00, -0.00	+0, -0	+0.001, -0.002	+-, ---	+0.001, -0.005				
(HG2)	0.52	17	0.052	1.00		0.256	0.522	0.01	680
	+0.02, -0.00	+2, -1	+0.003, -0.014	+-, ---		+0.021, -0.002	+0.030, -0.011		
<i>AREF 238 (HWMK 600)</i>									
450 nm	0.17	6	0.063	1.00	-0.149			0.01	680
(HG1)	+0.00, -0.00	+1, -1	+0.002, -0.002	+-, ---	+0.004, -0.004				
(HG2)	0.24	18	0.04	1.00		0.361	0.302	0	680
	+0.00, -0.02	+0, -4	+0.024, -0.001	+-, ---		+0.001, -0.013	+0.015, -0.005		
480 nm	0.24	14	0.06	1.00	-0.168			0.02	680
(HG1)	+0.00, -0.00	+1, -1	+0.002, -0.002	+-, ---	+0.004, -0.002				
(HG2)	0.32	23	0.043	1.00		0.326	0.377	0	680
	+0.00, -0.00	+0, -0	+0.003, -0.001	+-, ---		+0.001, -0.004	+0.005, -0.009		
530 nm	0.35	12	0.062	1.00	-0.139			0.03	680
(HG1)	+0.00, -0.00	+0, -0	+0.002, -0.002	+-, ---	+0.002, -0.004				
(HG2)	0.43	20	0.043	1.00		0.315	0.372	0.01	680
	+0.00, -0.00	+0, -0	+0.002, -0.002	+-, --		+0.005, -0.001	+0.006, -0.007		

(continued on next page)

Table 1 (continued)

Sample	$w$	$\bar{\theta}$ (°)	$h$	$B0$	$\zeta$	$b$	$c$	$\chi^2_{\text{red}}$	No.
600 nm	0.51	11	0.06	1.00	-0.143			0.02	680
(HG1)	+0.00, -0.00	+0, -0	+0.002, -0.001	+--, ---	+0.001, -0.002				
(HG2)	0.56	17	0.039	1.00		0.258	0.544	0.01	680
	+0.00, -0.00	+0, -0	+0.001, -0.001	+--, ---		+0.004, -0.002	+0.007, -0.009		
670 nm	0.55	11	0.06	1.00	-0.139			0.05	680
(HG1)	+0.00, -0.00	+0, -0	+0.002, -0.002	+--, ---	+0.003, -0.003				
(HG2)	0.62	17	0.032	1.00		0.295	0.472	0.01	680
	+0.00, -0.00	+0, -0	+0.001, -0.000	+--, ---		+0.004, -0.004	+0.007, -0.008		
750 nm	0.57	15	0.062	1.00	-0.147			0.08	640
(HG1)	+0.00, -0.00	+0, -0	+0.003, -0.006	+--, ---	+0.004, -0.006				
(HG2)	0.66	20	0.021	1.00		0.336	0.427	0.04	640
	+0.01, -0.00	+0, -0	+0.002, -0.001	+--, ---		+0.005, -0.005	+0.010, -0.009		
800 nm	0.59	15	0.054	1.00	-0.148			0.06	680
(HG1)	+0.00, -0.00	+1, -0	+0.011, -0.004	+--, ---	+0.009, -0.005				
(HG2)	0.67	21	0.018	1.00		0.331	0.438	0.02	680
	+0.00, -0.00	+0, -0	+0.002, -0.000	+--, ---		+0.003, -0.005	+0.006, -0.010		
860 nm	0.59	10	0.062	1.00	-0.116			0.04	640
(HG1)	+0.00, -0.00	+0, -0	+0.002, -0.002	+--, ---	+0.004, -0.002				
(HG2)	0.64	16	0.029	1.00		0.272	0.48	0.01	640
	+0.00, -0.00	+0, -0	+0.001, -0.000	+--, ---		+0.003, -0.003	+0.007, -0.006		
900 nm	0.61	5	0.054	1.00	-0.123			0.04	680
(HG1)	+0.00, -0.00	+2, -0	+0.014, -0.001	+--, ---	+0.011, -0.001				
(HG2)	0.66	13	0.036	0.98		0.263	0.498	0.01	680
	+0.00, -0.00	+0, -0	+0.003, -0.002	+--, ---		+0.006, -0.005	+0.012, -0.011		
930 nm	0.6	6	0.062	1.00	-0.11			0.05	680
(HG1)	+0.00, -0.00	+1, -1	+0.002, -0.002	+--, ---	+0.003, -0.002				
(HG2)	0.66	13	0.031	1.00		0.274	0.467	0.01	680
	+0.00, -0.00	+0, -0	+0.001, -0.000	+--, ---		+0.004, -0.003	+0.006, -0.006		
990 nm	0.62	8	0.06	1.00	-0.106			0.04	680
(HG1)	+0.00, -0.00	+1, -0	+0.004, -0.001	+--, ---	+0.005, -0.002				
(HG2)	0.67	15	0.028	0.98		0.271	0.47	0.01	680
	+0.00, -0.00	+0, -0	+0.001, -0.001	+--, ---		+0.006, -0.003	+0.011, -0.006		
<i>JSC1 (bulk)</i>									
450 nm	0.15	11	0.098	1.00	-0.068			0.01	680
(HG1)	+0.01, -0.01	+--, ---	+0.023, -0.058	+--, ---	+0.012, -0.065				
(HG2)	0.2	17	0.04	1.00		0.324	0.295	0	680
	+0.00, -0.00	+1, -1	+0.014, -0.002	+--, ---		+0.005, -0.009	+0.007, -0.020		
480 nm	0.19	15	0.064	1.00	-0.134			0.01	680
(HG1)	+0.00, -0.00	+1, -1	+0.004, -0.002	+--, ---	+0.005, -0.005				
(HG2)	0.26	23	0.048	1.00		0.337	0.299	0	680
	+0.01, -0.00	+1, -1	+0.003, -0.014	+--, ---		+0.017, -0.002	+0.018, -0.008		
530 nm	0.3	14	0.064	1.00	-0.119			0.02	680
(HG1)	+0.00, -0.00	+1, -0	+0.003, -0.002	+--, ---	+0.004, -0.004				
(HG2)	0.39	22	0.039	0.99		0.31	0.335	0	680
	+0.01, -0.00	+1, -0	+0.002, -0.010	+--, ---		+0.011, -0.004	+0.016, -0.009		
600 nm	0.46	13	0.063	1.00	-0.112			0.03	680
(HG1)	+0.00, -0.00	+1, -0	+0.004, -0.002	+--, ---	+0.005, -0.002				
(HG2)	0.54	20	0.022	1.00		0.295	0.422	0.01	680
	+0.00, -0.00	+0, -0	+0.002, -0.001	+--, ---		+0.003, -0.003	+0.006, -0.006		
670 nm	0.54	15	0.062	1.00	-0.123			0.04	680
(HG1)	+0.00, -0.00	+1, -0	+0.005, -0.003	+--, ---	+0.005, -0.005				
(HG2)	0.61	20	0.016	1.00		0.301	0.476	0.02	680
	+0.01, -0.01	+1, -0	+0.013, -0.000	+--, ---		+0.001, -0.011	+0.004, -0.021		
750 nm	0.61	15	0.054	1.00	-0.121			0.04	640
(HG1)	+0.00, -0.01	+0, -1	+0.014, -0.004	+--, ---	+0.010, -0.006				
(HG2)	0.68	20	0.019	0.93		0.301	0.446	0.02	640
	+0.00, -0.00	+0, -0	+0.004, -0.000	+--, ---		+0.004, -0.004	+0.010, -0.009		
800 nm	0.6	16	0.069	1.00	-0.101			0.06	680
(HG1)	+0.01, -0.00	+1, -0	+0.003, -0.019	+--, ---	+0.005, -0.012				
(HG2)	0.71	23	0.013	1.00		0.35	0.317	0.03	680
	+0.01, -0.01	+0, -1	+0.003, -0.000	+--, ---		+0.005, -0.005	+0.010, -0.007		
860 nm	0.66	10	0.064	1.00	-0.096			0.06	640
(HG1)	+0.00, -0.00	+1, -0	+0.004, -0.008	+--, ---	+0.006, -0.003				
(HG2)	0.73	16	0.021	0.96		0.294	0.413	0.02	640
	+0.00, -0.00	+0, -0	+0.004, -0.001	+--, ---		+0.004, -0.004	+0.008, -0.008		
900 nm	0.64	8	0.056	1.00	-0.092			0.05	680
(HG1)	+0.01, -0.00	+3, -0	+0.016, -0.006	+--, ---	+0.015, -0.002				
(HG2)	0.72	17	0.017	1.00		0.309	0.361	0.02	680
	+0.00, -0.00	+0, -0	+0.004, -0.000	+--, ---		+0.003, -0.004	+0.005, -0.006		
930 nm	0.62	13	0.065	1.00	-0.084			0.06	680
(HG1)	+0.00, -0.00	+0, -0	+0.005, -0.003	+--, ---	+0.005, -0.004				
(HG2)	0.69	18	0.013	1.00		0.323	0.37	0.02	680
	+0.00, -0.00	+0, -0	+0.002, -0.000	+--, ---		+0.003, -0.003	+0.006, -0.005		
990 nm	0.63	13	0.063	1.00	-0.087			0.05	680
(HG1)	+0.00, -0.00	+0, -0	+0.004, -0.003	+--, ---	+0.004, -0.004				

Table 1 (continued)

Sample	w	$\bar{\theta}$ (°)	h	B0	$\xi$	b	c	$\chi^2_{\nu}$	No.
(HG2)	0.71	19	0.016	1.00		0.315	0.368	0.02	680
	+0.00, -0.00	+0, -0	+0.002, -0.000	+--, ---		+0.003, -0.003	+0.006, -0.006		
<i>HWMK 600 (150–1000 <math>\mu\text{m}</math>)</i>									
450 nm	0.23	3	0.069	1.00	-0.091			0.02	680
(HG1)	+0.00, -0.00	+--, ---	+0.003, -0.003	+--, ---	+0.002, -0.007				
(HG2)	0.28	12	0.065	1.00		0.303	0.336	0.01	680
	+0.01, -0.02	+--, ---	+0.037, -0.031	+--, ---		+0.011, -0.002	+0.116, -0.003		
550 nm	0.35	0	0.063	1.00	-0.117			0.02	680
(HG1)	+0.00, -0.00	+--, ---	+0.003, -0.001	+--, ---	+0.004, -0.003				
(HG2)	0.37	6	0.06	1.00		0.244	0.527	0.01	680
	+0.01, -0.00	+--, ---	+0.004, -0.013	+--, ---		+0.011, -0.003	+0.045, -0.004		
750 nm	0.49	4	0.065	1.00	-0.11			0.03	680
(HG1)	+0.00, -0.00	+--, ---	+0.002, -0.007	+--, ---	+0.002, -0.006				
(HG2)	0.51	5	0.04	1.00		0.211	0.647	0.02	680
	+0.00, -0.00	+1, -1	+0.002, -0.001	+--, ---		+0.004, -0.004	+0.008, -0.009		
950 nm	0.49	1	0.067	1.00	-0.083			0.03	680
(HG1)	+0.00, -0.00	+--, ---	+0.003, -0.002	+--, ---	+0.004, -0.002				
(HG2)	0.51	3	0.034	1.00		0.224	0.557	0.02	680
	+0.00, -0.00	+--, ---	+0.002, -0.001	+--, ---		+0.003, -0.005	+0.005, -0.009		
<i>JSC1 (&lt;45 <math>\mu\text{m}</math>)</i>									
450 nm	0.35	0	0.077	1.00	0.035			0.05	680
(HG1)	+0.00, -0.00	+--, ---	+0.019, -0.003	+--, ---	+0.014, -0.006				
(HG2)	0.47	16	0.025	1.00		0.434	0.124	0.01	680
	+0.08, -0.01	+4, -0	+0.002, -0.002	+--, ---		+0.005, -0.005	+0.003, -0.003		
550 nm	0.63	2	0.078	1.00	0.019			0.11	680
(HG1)	+0.01, -0.00	+--, ---	+0.020, -0.011	+--, ---	+0.017, -0.007				
(HG2)	0.78	17	0.012	1.00		0.558	0.063	0.01	680
	+0.00, -0.00	+0, -0	+0.001, -0.000	+--, ---		+0.003, -0.004	+0.001, -0.001		
750 nm	0.87	0	0.062	1.00	0.008			0.17	680
(HG1)	+0.00, -0.00	+--, ---	+0.013, -0.004	+--, ---	+0.012, -0.005				
(HG2)	0.93	14	0.034	0.81		0.423	0.128	0.02	680
	+0.00, -0.01	+0, -1	+0.001, -0.019	+--, ---		+0.027, -0.009	+0.027, -0.007		
950 nm	0.89	3	0.069	1.00	0.038			0.19	680
(HG1)	+0.00, -0.00	+1, -2	+0.010, -0.002	+--, ---	+0.005, -0.005				
(HG2)	0.93	13	0.017	1.00		0.447	0.111	0.02	680
	+0.00, -0.00	+0, -0	+0.002, -0.000	+--, ---		+0.003, -0.004	+0.001, -0.003		
<i>Pahala ash</i>									
450 nm	0.35	3	0.07	1.00	-0.082			0.05	680
(HG1)	+0.00, -0.00	+--, ---	+0.003, -0.003	+--, ---	+0.004, -0.005				
(HG2)	0.42	12	0.041	1.00		0.339	0.303	0.01	680
	+0.00, -0.00	+0, -1	+0.005, -0.001	+--, ---		+0.001, -0.004	+0.003, -0.010		
550 nm	0.68	3	0.07	1.00	-0.068			0.11	680
(HG1)	+0.00, -0.00	+--, ---	+0.003, -0.003	+--, ---	+0.003, -0.002				
(HG2)	0.74	11	0.033	1.00		0.31	0.346	0.02	680
	+0.00, -0.00	+0, -0	+0.001, -0.001	+--, ---		+0.004, -0.004	+0.007, -0.008		
750 nm	0.9	2	0.067	1.00	-0.05			0.15	680
(HG1)	+0.00, -0.00	+--, ---	+0.004, -0.002	+--, ---	+0.004, -0.002				
(HG2)	0.91	5	0.03	1.00		0.27	0.408	0.03	680
	+0.00, -0.00	+1, -0	+0.001, -0.000	+--, ---		+0.004, -0.004	+0.005, -0.010		
950 nm	0.91	0	0.058	1.00	-0.025			0.2	680
(HG1)	+0.00, -0.00	+--, ---	+0.027, -0.002	+--, ---	+0.016, -0.010				
(HG2)	0.92	6	0.026	0.96		0.302	0.331	0.03	680
	+0.00, -0.00	+2, -1	+0.002, -0.006	+--, ---		+0.009, -0.007	+0.011, -0.013		
<i>SCB5</i>									
450 nm	0.86	0	0.082	1.00	0.041			0.18	680
(HG1)	+0.00, -0.00	+--, ---	+0.010, -0.006	+--, ---	+0.009, -0.006				
(HG2)	0.89	7	0.018	1.00		0.332	0.245	0.02	680
	+0.01, -0.00	+4, -1	+0.042, -0.004	+--, ---		+0.007, -0.003	+0.002, -0.030		
550 nm	0.91	2	0.088	1.00	0.072			0.21	680
(HG1)	+0.00, -0.00	+--, ---	+0.004, -0.008	+--, ---	+0.003, -0.006				
(HG2)	0.93	7	0.021	1.00		0.357	0.19	0.01	680
	+0.00, -0.00	+0, -0	+0.001, -0.001	+--, ---		+0.002, -0.002	+0.004, -0.002		
750 nm	0.95	2	0.086	1.00	0.104			0.21	680
(HG1)	+0.00, -0.00	+1, -2	+0.012, -0.005	+--, ---	+0.012, -0.006				
(HG2)	0.97	7	0.026	1.00		0.354	0.16	0.02	680
	+0.00, -0.00	+0, -0	+0.001, -0.000	+--, ---		+0.002, -0.004	+0.002, -0.004		
950 nm	0.97	0	0.095	1.00	0.158			0.22	680
(HG1)	+0.00, -0.00	+--, ---	+0.013, -0.012	+--, ---	+0.017, -0.013				
(HG2)	0.98	8	0.062	0.97		0.392	0.092	0.02	680
	+0.00, -0.00	+1, -2	+0.001, -0.043	+--, ---		+0.014, -0.005	+0.033, -0.003		
<i>SCB5 + spherules</i>									
450 nm	0.62	27	0.045	1.00	-0.154			0.65	680
(HG1)	+0.01, -0.01	+1, -1	+0.026, -0.013	+--, ---	+0.022, -0.019				

(continued on next page)

Table 1 (continued)

Sample	$w$	$\bar{\theta}$ (°)	$h$	$B0$	$\zeta$	$b$	$c$	$\chi^2_v$	No.
(HG2)	0.7	28	0.107	0.28		0.367	0.406	0.61	680
	+0.02, -0.02	+2, -2	+0.051, -0.106	+0.17, -0.20		+0.035, -0.026	+0.078, -0.034		
550 nm	0.67	27	0.035	0.95	-0.172			0.97	680
(HG1)	+0.01, -0.01	+1, -1	+0.025, -0.015	+-, ---	+0.028, -0.020				
(HG2)	0.76	27	0.008	0.45		0.401	0.397	0.9	680
	+0.01, -0.01	+1, -1	+0.026, -0.007	+-, ---		+0.011, -0.016	+0.022, -0.031		
750 nm	0.77	25	0.021	1.00	-0.187			1.4	680
(HG1)	+0.01, -0.01	+1, -1	+0.018, -0.005	+-, ---	+0.021, -0.015				
(HG2)	0.84	25	0.022	0		0.405	0.419	1.28	680
	+0.06, -0.01	+4, -1	+-, ---	+-, ---		+0.013, -0.035	+0.024, -0.098		
950 nm	0.78	24	0.02	1.00	-0.197			1.78	680
(HG1)	+0.01, -0.01	+1, -1	+0.016, -0.005	+-, ---	+0.021, -0.016				
(HG2)	0.93	24	0	0.8		0.801	0.029	1.57	680
	+0.00, -0.00	+1, -1	+-, ---	+-, ---		+0.005, -0.006	+0.001, -0.001		

“+-, ---” parameter is under-constrained by data.

(HG1) = 1-term Henyey–Greenstein model results; (HG2) = 2-term Henyey Greenstein model results (*in italics*).

$w$  = single-scattering albedo,  $\bar{\theta}$  = macroscopic roughness parameter,  $h$  = opposition effect width,  $B0$  = opposition effect height,  $\zeta$  = 1-term HG asymmetry parameter,  $b$  = 2-term HG asymmetry parameter,  $c$  = 2-term HG backscattering parameter,  $\chi^2_v$  = reduced chi-square error, No. = number of BUG observations.

ratios varied with phase angle in our samples (referred to here as ratio phase curves). This phenomenon was noted in early spectral studies of the Moon (e.g., Gehrels et al., 1964; Hapke and Kopal, 1971), and has recently been observed in data from the Lunar Reconnaissance Orbiter (LRO) wide-angle camera (Hapke et al., 2012). It has also been noted in telescopic data for Mercury (Warell and Bergfors, 2008) but not in MESSENGER spacecraft MDIS data. It has been observed in asteroids (e.g., Clark et al., 2002; Magrin et al., 2012; Sanchez et al., 2012), although Asteroid 44 Nysa actually becomes bluer with increasing phase angle (Rosenbush et al., 2009). Early laboratory studies also observed phase reddening of powdered rock samples up to phase angles of 30–60°, followed by the opposite effect at higher phase (e.g., Adams and Filice, 1967; Gradie et al., 1980). A similar result was reported by Schröder et al. (2011) for granular rock samples (for 600/500 nm and 500/400 nm ratios) and by Kaydash et al. (2010) for Apollo lunar soils, although Beck et al. (2012) reported steadily increasing 750/450 nm ratios with phase angle for meteorite powders. O’Leary and Briggs (1970) and Hapke et al. (1998) observed phase reddening for Apollo 11 soil, as did Akimov et al. (1979) and Shkuratov et al. (1999) for Luna soils. These authors also observed minima in ratio phase curves centered near 5–15°, at least for mare soils (Apollo 11, Luna 16 and 24). Shkuratov et al. (2011) referred to this as a “colorimetric opposition effect,” which has also been observed to varying degrees in Clementine (e.g., Shkuratov et al., 1999) and LRO wide-angle camera (WAC) data (Hapke et al., 2012).

Fig. 14 shows near-infrared/visible radiance factor ratios as a function of phase angle for all samples. Most of the Mars analog samples show initial phase reddening that falls off at phase angles varying from ~50° to 80°. The AREF 237 (HWMK 94) and SCB5 samples demonstrate flat to slightly reddening slopes with phase angle. The addition of spherules to the SCB5 soil causes in a slight increase in phase reddening. Most of the lunar analog soils show flat to slightly reddening slopes, whereas the MLS-1 (500–840  $\mu$ m) sample becomes bluer at high phase angles (>125°) and the JSC-1AF and Apollo soils exhibit slight falloffs near 55° and 80°, respectively. The 10084 Apollo 11 soil exhibits an increase in 750/450 nm ratio values at phase angles <10° (Fig. 15). This is an example of the color opposition effect (Shkuratov et al., 2011), and is not observed for the 68810 sample. Moreover, simple quadratic fits to the two soil plots demonstrate a crossover in phase reddening at about 38°, beyond which the 10084 soil exhibit a less red slope than the 68810 soil. This is similar to the results found by Kaydash et al. (2010) using the laboratory spectra of mare and highland Apollo soils from Pieters et al. (1991).

## 5. Discussion

### 5.1. Model parameter behaviors

Constraints on the modeled Hapke parameters vary among samples, depending on the parameter and the type of phase function used (Tables 1 and 2). As is often found in photometric modeling efforts, the single-scattering albedo  $w$  is the best constrained parameter. The shapes of the  $w$  spectra shown in Figs. 5 and 6 tend to mimic their spectral reflectance curves well (cf., Taylor et al., 2001; Hamilton et al., 2008). Values of  $w$  modeled using 1-term HG functions are consistently lower than those modeled using 2-term HG functions, as are macroscopic roughness ( $\bar{\theta}$ ) values. Conversely, the opposition effect width ( $h$ ) parameter values (when well constrained) are almost always lower for the 2-term HG models. This type of interplay among Hapke model parameters is similar to observations made by other workers (e.g., Goguen et al., 2010; Shepard and Helfenstein, 2011).

Fine-grained samples tend to have higher  $w$  values than their coarse-grained counterparts (e.g., JSC-1 (<45  $\mu$ m), JSC-1AF) and the lowest  $\bar{\theta}$  values (e.g., SCB5 soil, Pahala ash). Cord et al. (2003) and Helfenstein and Shepard (2007) both observed a decrease in  $\bar{\theta}$  values with decreasing grain size in their laboratory studies, and Shepard and Helfenstein (2007) suggest that bright surfaces should appear smoother than dark surfaces, consistent with the results shown in Fig. 7. Further, Fig. 7 demonstrates little wavelength dependency with  $\bar{\theta}$  except for the Pahala ash, FJS-1, and MLS-1 (<1 mm and 500–840  $\mu$ m) samples, which show a >5° decrease in roughness with increasing wavelength.

The only sample that exhibits appreciable change in  $h$  values with wavelength (as modeled from 1-term HG solutions) is the SCB5 soil with spherules. This sample shows decreased  $h$  values with wavelength (Fig. 8) relative to the other samples for reasons that may be related to its high  $\bar{\theta}$  values and bimodal grain size distribution. Some of the highest  $h$  values are exhibited by the fine-grained soils (SCB5, Pahala ash, JSC-1 (<45  $\mu$ m), JSC-1AF, FJS-1). Larger  $h$  values previously would have been considered normal for less porous samples and/or samples with a more uniform grain size distribution, consistent with these soils. However, as described above recent work suggests that such physical interpretations should not be rigorously applied on the basis of Hapke modeling (e.g., Helfenstein and Shepard, 2011; Shepard and Helfenstein, 2011).

Opposition effect magnitude ( $B0$ ) values are under-constrained in all models, but they are equal to our imposed limit of 1.0 for the

**Table 2**  
Hapke model results for lunar analog and Apollo soils.

Sample	w	$\bar{\theta}$ (°)	h	B0	$\xi$	b	c	$\chi^2_V$	No.
<i>FJS-1</i>									
410 nm	0.49	0	0.092	1.00	0.041			0.04	680
(HG1)	+0.00, -0.00	+,-,-	+0.003, -0.011	+,-,-	+0.002, -0.008				
(HG2)	0.55	12	0.022	0.98		0.305	0.236	0.01	680
	+0.00, -0.00	+0, -0	+0.006, -0.002	+,-,-		+0.004, -0.005	+0.005, -0.006		
550 nm	0.55	0	0.074	1.00	0.042			0.04	680
(HG1)	+0.00, -0.00	+,-,-	+0.028, -0.000	+,-,-	+0.014, -0.004				
(HG2)	0.59	7	0.023	1.00		0.271	0.28	0.01	680
	+0.00, -0.00	+0, -0	+0.004, -0.001	+,-,-		+0.004, -0.004	+0.005, -0.006		
750 nm	0.59	2	0.09	1.00	0.065			0.05	680
(HG1)	+0.00, -0.00	+,-,-	+0.003, -0.004	+,-,-	+0.003, -0.004				
(HG2)	0.63	5	0.023	1.00		0.264	0.269	0.01	680
	+0.00, -0.00	+1, -0	+0.002, -0.001	+,-,-		+0.005, -0.003	+0.005, -0.005		
950 nm	0.55	2	0.093	1.00	0.074			0.05	680
(HG1)	+0.00, -0.00	+,-,-	+0.007, -0.004	+,-,-	+0.004, -0.004				
(HG2)	0.58	6	0.021	1.00		0.283	0.251	0.01	680
	+0.00, -0.00	+0, -0	+0.001, -0.001	+,-,-		+0.004, -0.004	+0.004, -0.005		
<i>JSC-1 (&lt;1 mm)</i>									
410 nm	0.25	13	0.067	1.00	-0.074			0.03	680
(HG1)	+0.00, -0.00	+1, -0	+0.011, -0.002	+,-,-	+0.009, -0.003				
(HG2)	0.32	20	0.076	0.92		0.332	0.237	0.01	680
	+0.03, -0.01	+2, -1	+0.007, -0.059	+,-,-		+0.044, -0.007	(+0.065, -0.012)		
550 nm	0.33	13	0.076	1.00	-0.039			0.04	680
(HG1)	+0.00, -0.00	+1, -1	+0.005, -0.002	+,-,-	+0.006, -0.005				
(HG2)	0.42	20	0.074	0.68		0.365	0.202	0.01	680
	+0.05, -0.02	+2, -2	+0.007, -0.062	+0.32, -0.18		+0.042, -0.007	(+0.061, -0.008)		
750 nm	0.38	14	0.079	1.00	-0.023			0.06	680
(HG1)	+0.00, -0.00	+0, -1	+0.006, -0.011	+,-,-	+0.005, -0.006				
(HG2)	0.52	22	0.01	1.00		0.432	0.161	0.02	680
	+0.14, -0.01	+4, -1	+0.001, -0.010	+,-,-		+0.006, -0.005	(+0.005, -0.005)		
950 nm	0.37	13	0.077	1.00	-0.011			0.06	680
(HG1)	+0.00, -0.00	+1, -1	+0.010, -0.005	+,-,-	+0.008, -0.005				
(HG2)	0.64	20	0.128	0.05		0.78	0.014	0.02	680
	+0.00, -0.00	+1, -1	+,-,-	+,-,-		+0.006, -0.014	(+0.000, -0.003)		
<i>JSC-1A</i>									
410 nm	0.23	12	0.08	1.00	-0.02			0.02	680
(HG1)	+0.00, -0.00	+1, -0	+0.007, -0.007	+,-,-	+0.008, -0.006				
(HG2)	0.31	20	0.016	0.95		0.379	0.21	0.01	680
	+0.01, -0.01	+1, -1	+0.337, -0.001	+,-,-		+0.006, -0.007	+0.007, -0.060		
550 nm	0.31	12	0.083	1.00	0.001			0.04	680
(HG1)	+0.00, -0.00	+1, -0	+0.011, -0.005	+,-,-	+0.008, -0.004				
(HG2)	0.42	20	0.1	0.39		0.41	0.156	0.02	680
	+0.15, -0.04	+5, -2	+,-,-	+,-,-		+0.033, -0.033	+0.037, -0.062		
750 nm	0.65	26	0.113	1.00	0.701			0.06	680
(HG1)	+0.02, -0.32	+,-,-	+,-,-	+,-,-	+0.271, -0.765				
(HG2)	0.63	18	0	0.13		0.812	0.009	0.01	680
	+0.00, -0.00	+0, -0	+,-,-	+,-,-		+0.001, -0.001	+0.000, -0.000		
950 nm	0.35	12	0.075	1.00	0.033			0.05	680
(HG1)	+0.01, -0.01	+1, -1	+0.030, -0.002	+,-,-	+0.918, -0.005				
(HG2)	0.57	22	0.001	0		0.611	0.045	0.02	680
	+0.07, -0.00	+1, -9	+,-,-	+,-,-		+0.012, -0.004	+0.001, -0.013		
<i>JSC-1AF</i>									
410 nm	0.38	9	0.099	1.00	0.088			0.04	680
(HG1)	+0.00, -0.00	+1, -0	+0.007, -0.004	+,-,-	+0.005, -0.004				
(HG2)	0.48	15	0.011	0.99		0.405	0.145	0.01	680
	+0.16, -0.01	+5, -0	+0.003, -0.011	+,-,-		+0.004, -0.005	+0.003, -0.062		
550 nm	0.53	9	0.103	1.00	0.116			0.07	680
(HG1)	+0.22, -0.00	+1, -0	+0.010, -0.005	+,-,-	+0.750, -0.004				
(HG2)	0.72	14	0.002	0.84		0.707	0.018	0.01	680
	+0.00, -0.00	+0, -0	+0.006, -0.001	+,-,-		+0.003, -0.046	+0.000, -0.006		
750 nm	0.57	2	0.09	1.00	0.083			0.09	680
(HG1)	+0.18, -0.01	+,-,-	+0.112, -0.043	+,-,-	+0.810, -0.027				
(HG2)	0.76	14	0.063	0.05		0.719	0.017	0.01	680
	+0.00, -0.01	+1, -0	+,-,-	+,-,-		+0.004, -0.039	+0.000, -0.005		
950 nm	0.59	10	0.109	1.00	0.133			0.09	680
(HG1)	+0.17, -0.00	+11, -1	+0.010, -0.009	+,-,-	+0.765, -0.007				
(HG2)	0.76	13	0.136	0.87		0.723	0.009	0.01	680
	+0.00, -0.00	+0, -1	+,-,-	+0.08, -0.76		+0.011, -0.005	+0.004, -0.000		
<i>MLS-1 (500–840 <math>\mu</math>m)</i>									
410 nm	0.31	11	0.074	1.00	0.009			0.02	680
(HG1)	+0.01, -0.00	+1, -0	+0.017, -0.002	+,-,-	+0.007, -0.003				
(HG2)	0.57	25	0.004	0.98		0.674	0.023	0	680
	+0.00, -0.00	+0, -0	+0.001, -0.001	+,-,-		+0.004, -0.004	+0.000, -0.000		

(continued on next page)

Table 2 (continued)

Sample	w	$\bar{\theta}$ (°)	h	B0	$\zeta$	b	c	$\chi^2_{\nu}$	No.
550 nm	0.34	11	0.079	0.99	0.03			0.03	680
(HG1)	+0.01, -0.01	+1, -3	+0.023, -0.011	+-----	+0.021, -0.012				
(HG2)	0.55	24	0.008	1.00		0.571	0.045	0.01	680
	+0.03, -0.00	+1, -1	+0.047, -0.007	+-----		+0.013, -0.003	+0.002, -0.001		
750 nm	0.34	10	0.089	1.00	0.057			0.03	680
(HG1)	+0.00, -0.00	+1, -1	+0.006, -0.005	+-----	+0.005, -0.005				
(HG2)	0.6	20	0.151	0		0.741	0.014	0	680
	+0.00, -0.00	+0, -0	+-----	+-----		+0.000, -0.004	+0.000, -0.000		
950 nm	0.3	8	0.092	1.00	0.066			0.03	680
(HG1)	+0.00, -0.00	+1, -1	+0.007, -0.008	+-----	+0.008, -0.005				
(HG2)	0.56	19	0.001	0.69		0.746	0.014	0	680
	+0.00, -0.00	+0, -0	+-----	+-----		+0.002, -0.004	+0.000, -0.004		
<i>MLS-1 (&lt;1 mm)</i>									
410 nm	0.51	15	0.084	1.00	0.016			0.07	680
(HG1)	+0.00, -0.00	+1, -0	+0.004, -0.010	+-----	+0.005, -0.008				
(HG2)	0.71	22	0.5	0.59		0.628	0.028	0.02	680
	+0.05, -0.00	+1, -6	+-----	+-----		+0.066, -0.006	+0.011, -0.004		
550 nm	0.6	13	0.077	1.00	0.026			0.08	680
(HG1)	+0.00, -0.00	+1, -0	+0.011, -0.003	+-----	+0.007, -0.006				
(HG2)	0.79	18	0.148	0.51		0.753	0.012	0.02	680
	+0.01, -0.00	+1, -2	+-----	+-----		+0.033, -0.010	+0.004, -0.000		
750 nm	0.61	13	0.063	1.00	0.03			0.08	680
(HG1)	+0.01, -0.01	+1, -1	+0.040, -0.001	+-----	+0.031, -0.006				
(HG2)	0.8	16	0.009	0.15		0.786	0.012	0.01	680
	+0.00, -0.00	+0, -1	+-----	+-----		+0.006, -0.012	+0.000, -0.002		
950 nm	0.58	13	0.084	1.00	0.058			0.08	680
(HG1)	+0.00, -0.00	+0, -0	+0.008, -0.005	+-----	+0.006, -0.006				
(HG2)	0.78	15	0.002	0		0.794	0.011	0.01	680
	+0.00, -0.00	+0, -0	+-----	+-----		+0.001, -0.001	+0.000, -0.000		
<i>MLS-1 (glass)</i>									
410 nm	0.21	12	0.093	1.00	0.102			0.02	680
(HG1)	+0.27, -0.00	+22, -1	+0.015, -0.010	+-----	+0.862, -0.010				
(HG2)	0.44	21	0.232	0		0.758	0.011	0	680
	+0.00, -0.00	+0, -1	+-----	+-----		+0.001, -0.002	+0.000, -0.000		
550 nm	0.21	10	0.1	1.00	0.099			0.02	680
(HG1)	+0.26, -0.00	+22, -1	+0.005, -0.008	+-----	+0.854, -0.007				
(HG2)	0.42	23	0.001	0		0.666	0.024	0	680
	+0.04, -0.00	+1, -6	+-----	+-----		+0.005, -0.002	+0.000, -0.010		
750 nm	0.23	7	0.097	1.00	0.101			0.02	680
(HG1)	+0.25, -0.00	+24, -1	+0.008, -0.010	+-----	+0.796, -0.007				
(HG2)	0.45	20	0.207	0.69		0.709	0.01	0	680
	+0.02, -0.01	+2, -2	+-----	+-----		+0.060, -0.022	+0.006, -0.000		
950 nm	0.21	2	0.103	1.00	0.106			0.02	680
(HG1)	+0.26, -0.00	+-----	+0.015, -0.010	+-----	+0.824, -0.011				
(HG2)	0.45	18	0.099	0.07		0.763	0.01	0	680
	+0.00, -0.00	+0, -1	+-----	+-----		+0.006, -0.006	+0.000, -0.001		
<i>Apollo 11 10084</i>									
410 nm	0.21	0	0.05	1.00	-0.109			0.02	769
(HG1)	+0.01, -0.01	+-----	+0.056, -0.007	+-----	+0.040, -0.014				
(HG2)	0.27	14	0.035	1.00		0.343	0.309	0	769
	+0.00, -0.00	+0, -0	+0.003, -0.001	+-----		+0.005, -0.004	+0.007, -0.007		
550 nm	0.25	7	0.07	1.00	-0.086			0.03	769
(HG1)	+0.00, -0.00	+1, -1	+0.004, -0.003	+-----	+0.005, -0.005				
(HG2)	0.31	14	0.034	1.00		0.343	0.299	0	769
	+0.00, -0.00	+0, -0	+0.003, -0.001	+-----		+0.004, -0.005	+0.007, -0.005		
750 nm	0.3	7	0.071	1.00	-0.075			0.04	769
(HG1)	+0.00, -0.00	+1, -1	+0.003, -0.003	+-----	+0.005, -0.004				
(HG2)	0.38	14	0.032	1.00		0.343	0.293	0	769
	+0.00, -0.00	+0, -0	+0.002, -0.001	+-----		+0.005, -0.004	+0.007, -0.005		
950 nm	0.31	2	0.07	1.00	-0.071			0.04	769
(HG1)	+0.01, -0.00	+-----	+0.022, -0.017	+-----	+0.022, -0.012				
(HG2)	0.39	14	0.035	1.00		0.338	0.29	0	769
	+0.01, -0.00	+1, -0	+0.003, -0.004	+-----		+0.009, -0.002	+0.006, -0.010		
<i>Apollo 16 68810</i>									
410 nm	0.38	7	0.054	1.00	-0.13			0.1	765
(HG1)	+0.00, -0.01	+3, -1	+0.019, -0.001	+-----	+0.014, -0.007				
(HG2)	0.45	15	0.042	1.00		0.325	0.367	0.01	765
	+0.00, -0.00	+0, -0	+0.002, -0.003	+-----		+0.006, -0.003	+0.011, -0.006		
550 nm	0.44	7	0.062	1.00	-0.115			0.1	765
(HG1)	+0.00, -0.00	+1, -1	+0.010, -0.001	+-----	+0.007, -0.002				
(HG2)	0.52	15	0.035	1.00		0.334	0.347	0.01	765
	+0.00, -0.00	+0, -0	+0.002, -0.001	+-----		+0.004, -0.003	+0.006, -0.005		
750 nm	0.52	8	0.069	1.00	-0.092			0.1	765
(HG1)	+0.00, -0.00	+0, -1	+0.003, -0.007	+-----	+0.002, -0.008				

Table 2 (continued)

Sample	$w$	$\bar{\theta}$ (°)	$h$	$B0$	$\xi$	$b$	$c$	$\chi^2_r$	No.
(HG2)	0.6	15	0.029	0.99		0.337	0.333	0.02	765
	+0.00, -0.00	+0, -0	+0.002, -0.001	+--,-		+0.005, -0.005	+0.006, -0.008		
950 nm	0.56	7	0.065	1.00	-0.086			0.1	765
(HG1)	+0.00, -0.00	+1, -0	+0.005, -0.002	+--,-	+0.005, -0.004				
(HG2)	0.65	15	0.023	0.98		0.353	0.31	0.02	765
	+0.00, -0.00	+0, -0	+0.002, -0.003	+--,-		+0.005, -0.005	+0.008, -0.008		

“+--,-” parameter is under-constrained by data.

(HG1) = 1-term Henyey–Greenstein model results; (HG2) = 2-term Henyey Greenstein model results (*in italics*).

$w$  = single-scattering albedo,  $\bar{\theta}$  = macroscopic roughness parameter,  $h$  = opposition effect width,  $B0$  = opposition effect height,  $\xi$  = 1-term HG asymmetry parameter,  $b$  = 2-term HG asymmetry parameter,  $c$  = 2-term HG backscattering parameter,  $\chi^2_r$  = reduced chi-square error, No. = number of BUG observations.

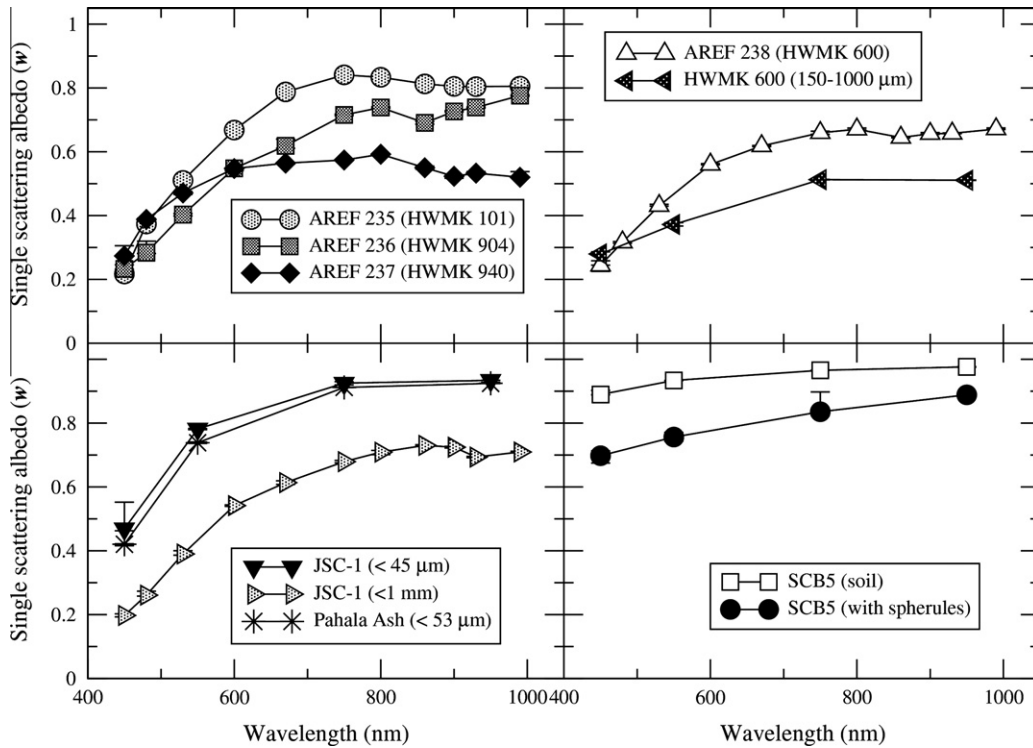


Fig. 5. Single-scattering albedo spectra for Mars analog soils, modeled from 2-term Henyey–Greenstein functions for all samples (Table 1).

Apollo soils and all Mars analog soils except for the SCB5 soil with spherules (particularly from the 2-term HG model results). However,  $B0$  values for the lunar analog samples are more often  $<1.0$  (albeit under-constrained), with the MLS-1 glass sample having the lowest average  $B0$  value of all samples (0.19). Although these low values may imply that these samples allow more internal scattering (lower opacity), the lack of well-constrained model results for  $B0$  values limits this interpretation.

Fig. 9 demonstrates that increases in the 1-term HG asymmetry parameter ( $\xi$ ) with wavelength are apparent for some samples (e.g., Pahala ash, AREF 237 (HWMK 940), SCB5 soil, JSC-1, JSC-1A), but only the SCB5 soil with spherules exhibits a decrease (greater backscattering) with wavelength. By comparison the 2-term HG model results show an increase in forward scattering with wavelength (Fig. 13) for both SCB5 samples as well as the JSC-1, JSC-1A, and to a lesser extent both Apollo soils. Minor increases in backscattering with wavelength are observed for the AREF 235 (HWMK 101) and AREF 238 (HWMK 600) samples, although with variations among the different wavelengths.

We note that analyses of the lunar JSC-1 sample by Gunderson et al. (2006) modeled  $w$ ,  $h$  and  $\bar{\theta}$  values smaller than those

presented here. Also, their 2-term HG  $b$ ,  $c$  values are indicative of a broader, more backscattering sample than shown here. These differences may result because they prepared their sample by “sprinkling 1–2 mm of loose material over a packed surface” or because of their lack of phase angle coverage  $>85^\circ$ .

### 5.2. Results from 2-term HG phase functions

The 2-term HG phase function parameter plots in Figs. 10 and 11 demonstrate interesting overall trends in the samples. Samples with fewer fine-grained components were more broadly backscattering (low  $b$ , high  $c$  values). The AREF/HWMK, JSC-1 (<1 mm), and Pahala ash Mars analog samples (Fig. 10) fall within a region encompassing the agglutinate particles, clear spheres, and spheres with a moderate density of internal scatterers from McGuire and Hapke (1995). MER Spirit results from three representative areas (Johnson et al., 2006a) range from granular soils near the landing site and in the Gusev plains to the macroscopically smoother soils near the base of Husband Hill. The SCB5 soil and JSC-1 (<45 μm) samples were more narrowly forward scattering, consistent with the smooth surface of these fine-grained samples.

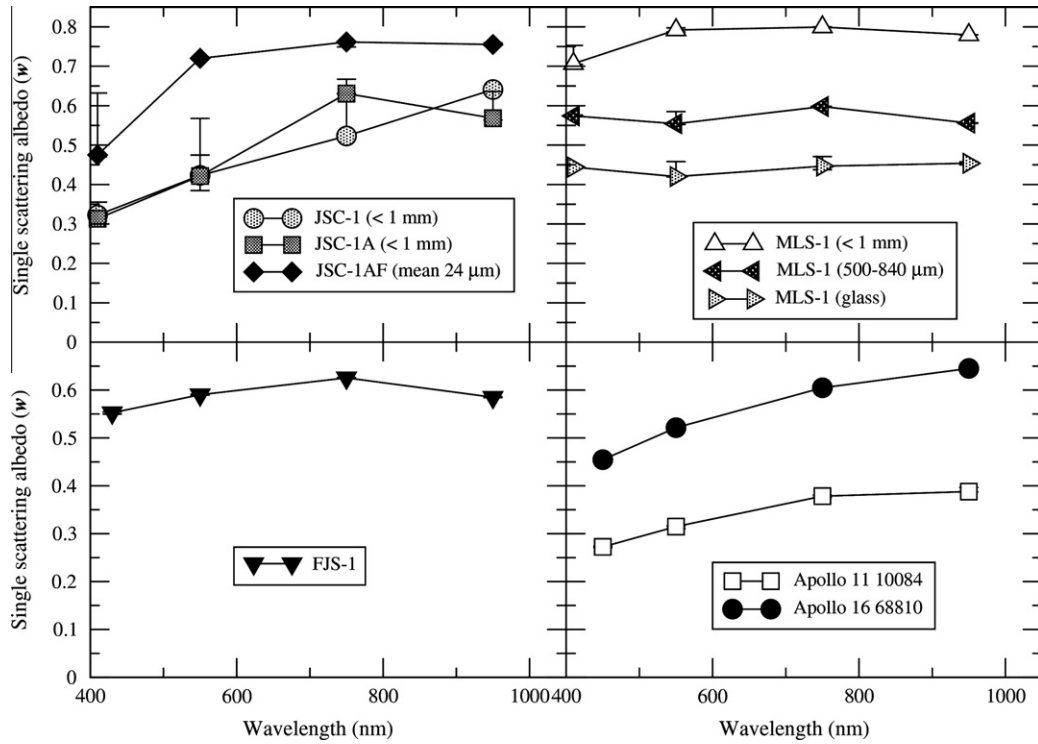


Fig. 6. Single-scattering albedo spectra for lunar analog soils, modeled from 2-term Henyey–Greenstein functions for all samples (Table 2).

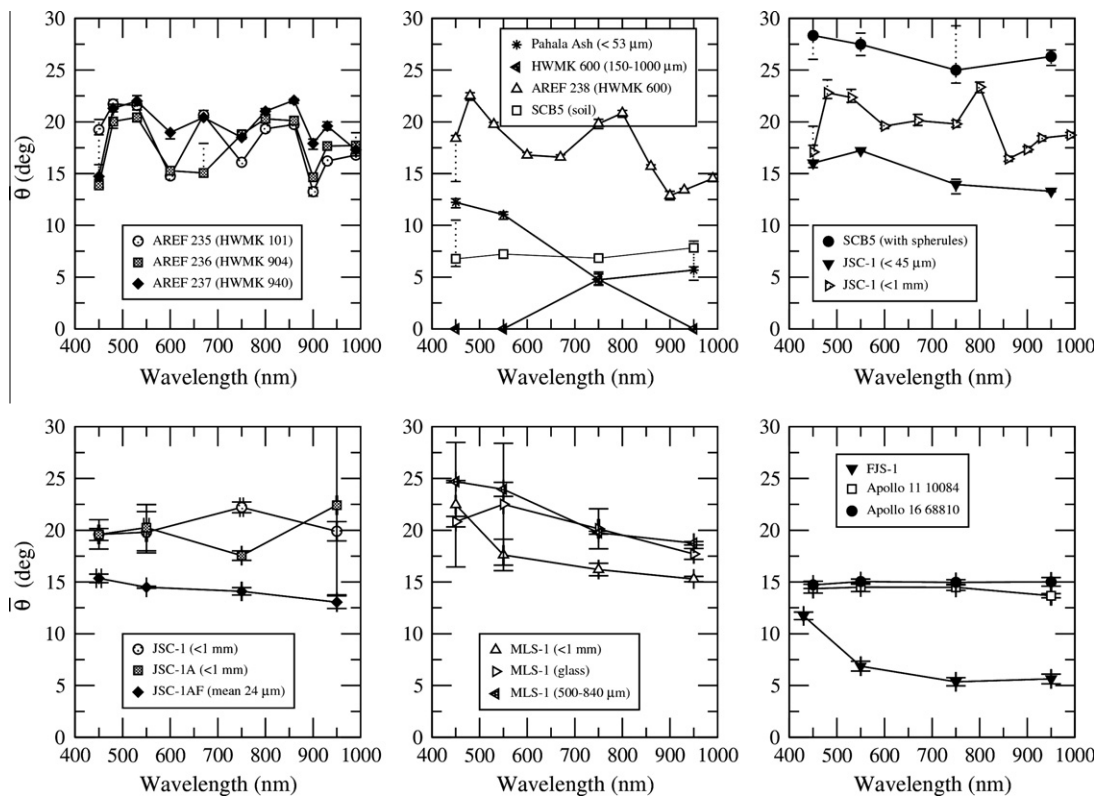


Fig. 7. Variation of roughness parameter ( $\bar{\theta}$ ) values with wavelength for all samples from 2-term HG models. Under-constrained model results for 3 wavelengths of the HWMK 600 data 1044 are shown with values of 0.0.

Among the lunar analog samples, the JSC-1AF sample exhibits higher  $w$  values than its coarser-grained JSC-1A split, as expected. The high  $w$  values for the  $<1$  mm fraction of MLS-1 are consistent

with the significant fine-grained fraction in this split compared to the 500–840  $\mu\text{m}$  split. Most of the lunar analog 2-term HG phase functions fall in the narrow, forward-scattering lobe in Fig. 11,

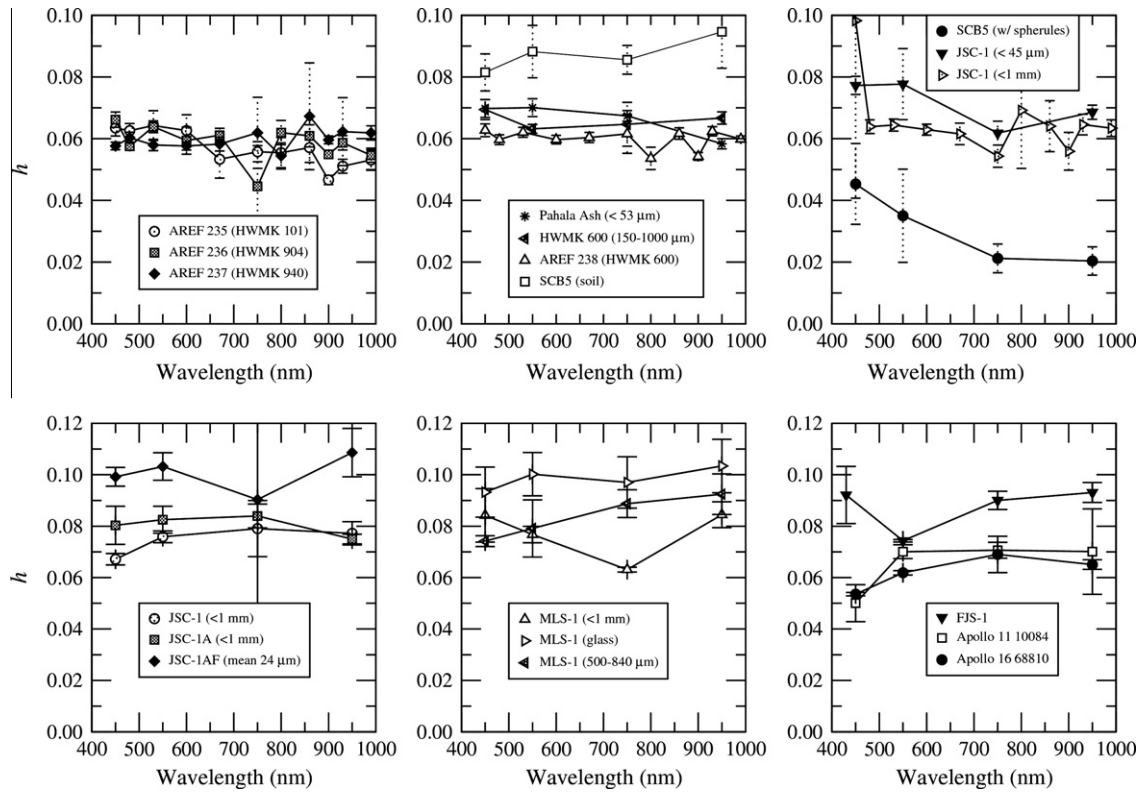


Fig. 8. Variation of opposition effect width ( $h$ ) parameter values with wavelength for all samples from 1-term HG models.

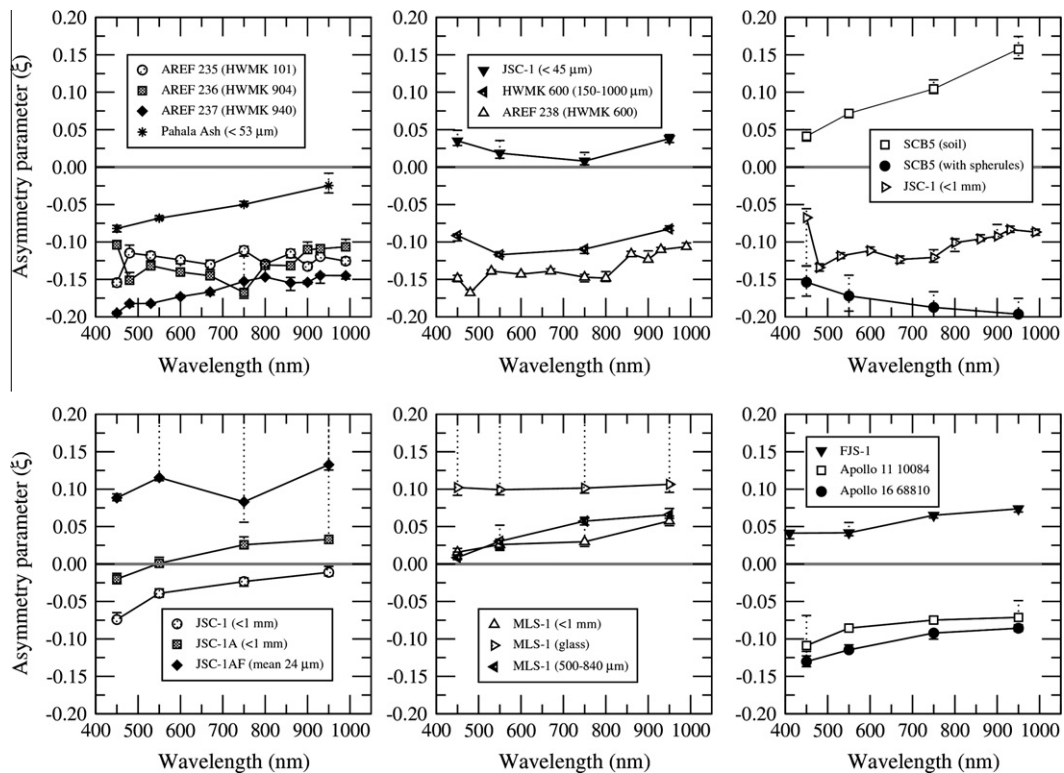
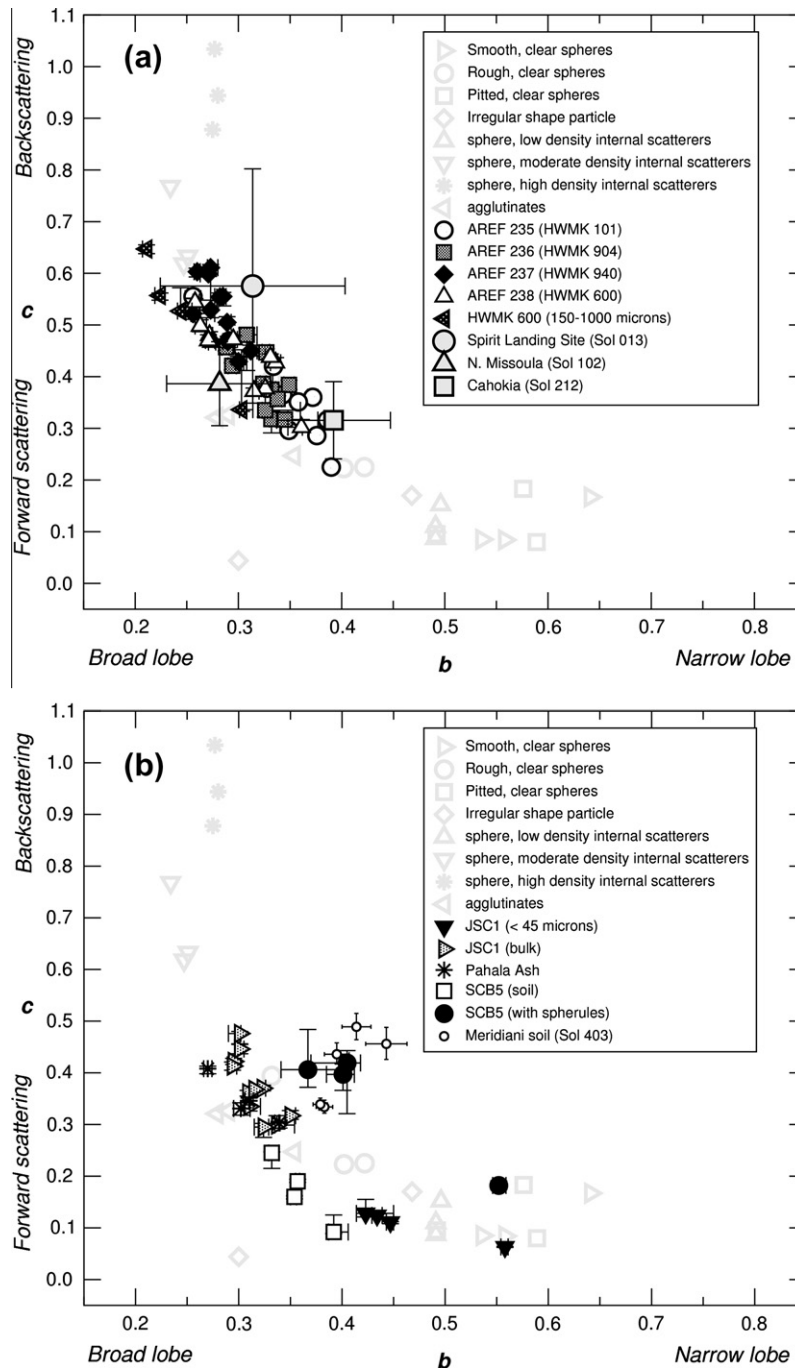


Fig. 9. Asymmetry parameter ( $\xi$ ) values modeled from 1-term Henyey–Greenstein functions for all samples as a function of wavelength. Gray lines at  $\xi = 0$  delineate forward scattering ( $\xi > 0$ ) from backscattering ( $\xi < 0$ ) behavior.

similar to the spheres of various surface textures with a low density of internal scatterers from McGuire and Hapke (1995). The

FJS-1, JSC-1, and JSC-1A were more broadly backscattering (low  $b$ , high  $c$  values) than the other samples.



**Fig. 10.** Parameters  $b$  and  $c$  modeled from 2-term Henyey–Greenstein functions for Mars analog samples, compared to experimental results for artificial particles from McGuire and Hapke (1995) and to MER Pancam results for representative Spirit (Johnson et al., 2006a) and Opportunity for (Johnson et al., 2006b) soils.

As noted above, some samples exhibit spectral variability in their  $b$  and  $c$  values, or include the presence of outlier points for some wavelengths (Figs. 10–13). These apparent aberrations were investigated by performing additional model runs in which starting values were varied; however, the same solutions were obtained repeatedly. Comparison of all modeled parameters demonstrated that under-constrained solutions for  $h$  values are sometimes correlated with outlier points, suggesting that such points are the result of relatively weak constraints on the overall model results.

Also of interest are samples modeled with  $b > 0.6$  and  $c < 0.1$ , a region not represented by the samples studied by McGuire and Hapke (1995). Fig. 11 demonstrates that the many of the JSC and

MLS lunar analog samples tend to plot in this region, indicative of very narrowly forward-scattering materials. Repeated modeling attempts using alternate starting conditions (or fixed values for some parameters) resulted in the same modeled  $b$ ,  $c$  parameters. Hapke models from other workers have shown results occupying this region in  $b$ ,  $c$  space. For example, the MER Pancam models from Johnson et al. (2006a,b) reported low  $c$ /high  $b$  values for some dust-poor (“gray”) rocks and one dusty soil (Paso Robles prior to a dust-cleaning event on Husband Hill at the Spirit site), as well as some rover tracks from the Opportunity site. In their models of High Resolution Stereo Experiment (HRSC) orbital data of Gusev Crater, Jehl et al. (2011) also reported that one unit exhibited low

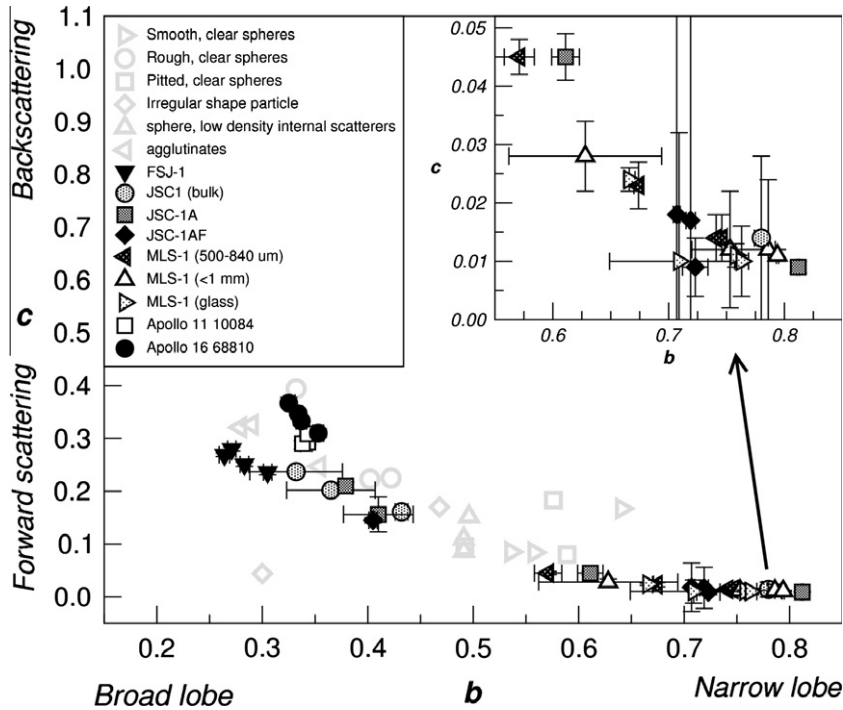


**Fig. 11.** Parameters  $b$  and  $c$  modeled from 2-term Henyey–Greenstein functions for lunar analog samples, compared to experimental results for artificial particles from McGuire and Hapke (1995). Inset shows detail of low  $c$ /high  $b$  valued results.

$c$ /high  $b$  values. This unit was modeled with the lowest macroscopic roughness and highest  $w$  values of all units. Combined with the unit's sporadic distribution with the region studied, this lead Jehl et al. (2008) to suggest that the materials were preserved lay-

ers of find-grained surface dust. Souchon et al. (2011) also found that laboratory samples composed of >30% isolated translucent monocrystals and/or fresh glass particles exhibited low  $c$  and high  $b$  values. Beck et al. (2012) report similar values in their models of

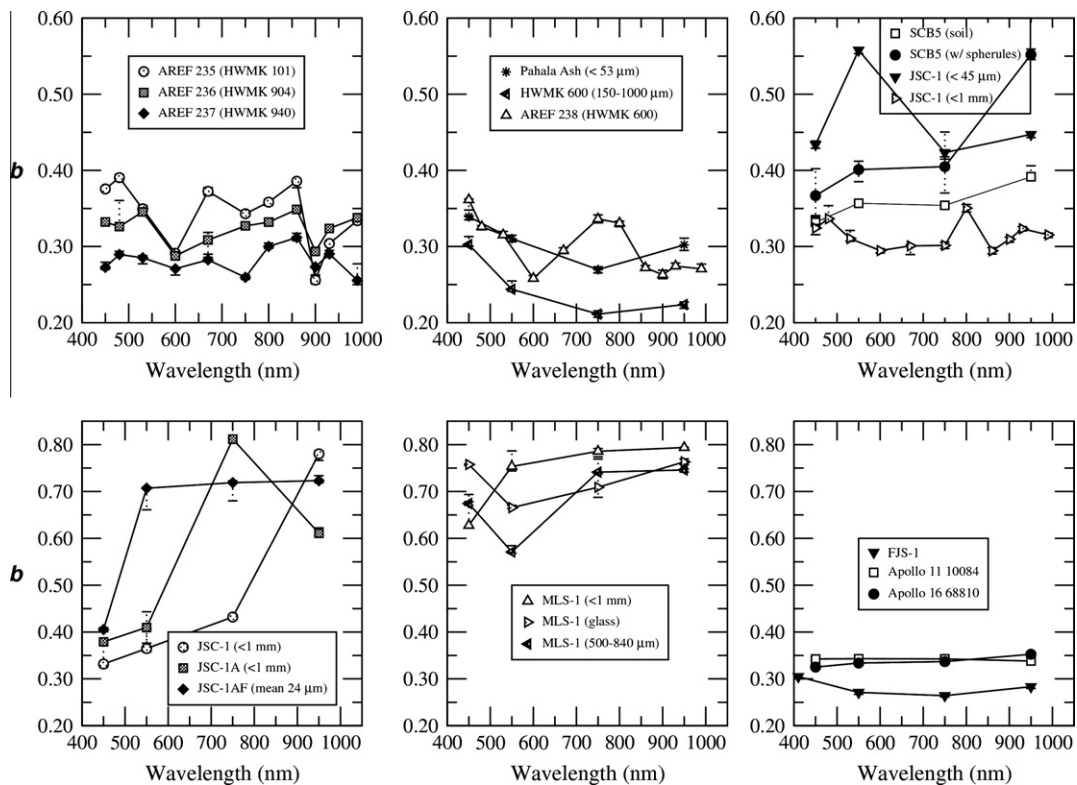


**Fig. 12.** Spectral variability of 2-term HG  $b$  parameter for all samples.

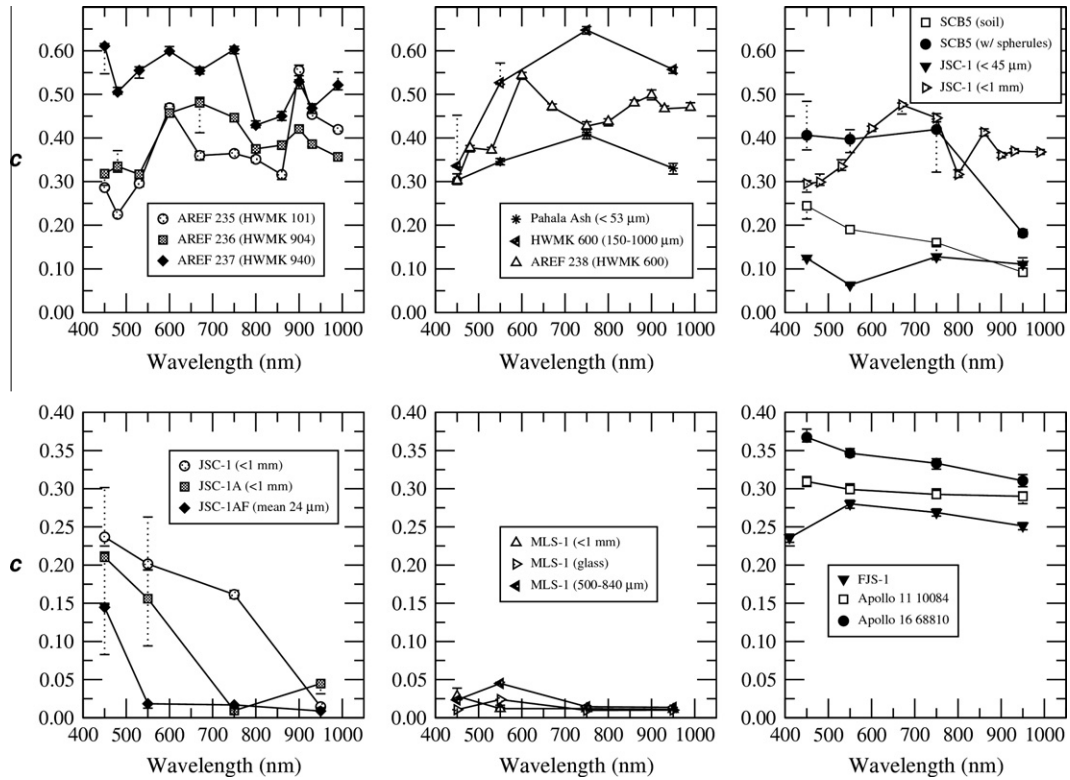


Fig. 13. Spectral variability of 2-term HG c parameter for all samples.

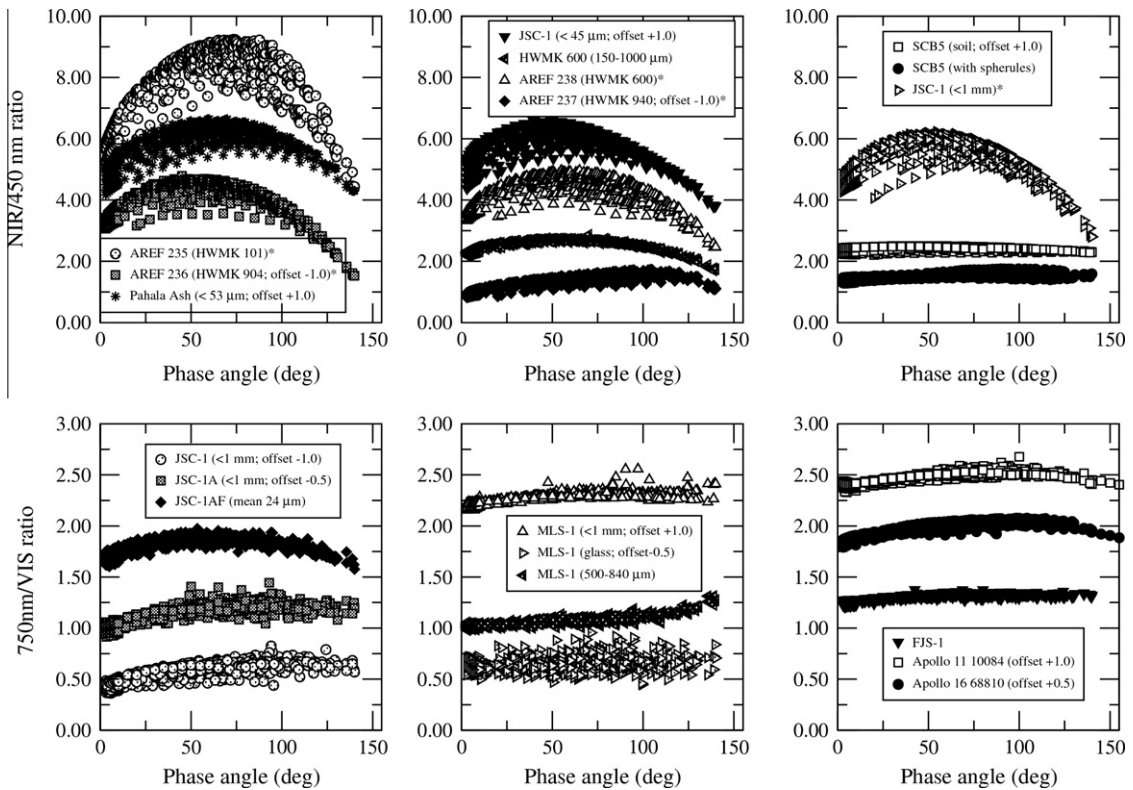
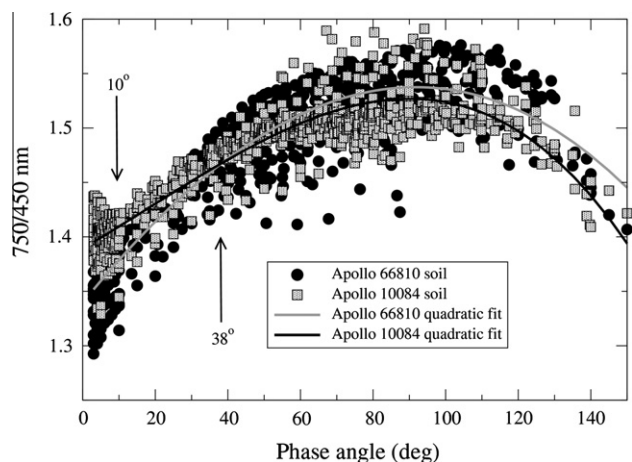


Fig. 14. Ratio of near-infrared to visible radiance factor values as a function of phase angle. Mars analog soils (top row) represent 750/450 nm ratios, except for AREF/HWMK and JSC-1 samples that represent 800/450 nm ratios (asterisk in legend name). Lunar analog soils represent 750/410 nm ratios, whereas Apollo soils represent 750/450 nm ratios. Offsets shown in legends where applicable.



**Fig. 15.** Ratio of near-infrared to visible radiance factor values as a function of phase angle for Apollo 11 and 16 soil samples, showing crossover near  $38^\circ$  between the two samples, as well as an upturn shortward of  $\sim 10^\circ$  phase angle for the 10084 sample.

meteorite powders for the C1 chondrite Orgueil, the HED eucrite Millbillillie, and the lunar meteorite MAC 88105. However, additional measurements are needed to further reconcile the properties of particles from which model results occupy this region of  $b$ ,  $c$  space.

### 5.3. Spherule experiment

Comparison of the SCB5 samples with and without the added spherules is particularly interesting. Upon addition of the spherules,  $w$  decreased substantially (Fig. 5), and the average  $\bar{\theta}$  increased from  $7^\circ$  to  $26^\circ$ , the highest value of all samples studied here and comparable to the values modeled for spherule-rich soils from MER Opportunity data within Eagle and Endurance craters (Johnson et al., 2006b). For comparison,  $\bar{\theta}$  values modeled for soils from MER Spirit and Mars Pathfinder data ranged from  $\sim 2^\circ$  to  $19^\circ$  (Johnson et al., 1999, 2006a). The 1-term HG  $h$  value also decreased from 0.088 to 0.030 with the addition of spherules (the lowest of any sample), consistent with the less uniform grain size distribution of the spherule-rich sample (Fig. 8). The average 1-term HG asymmetry parameter ( $\xi$ ) changed from very forward scattering ( $+0.094$ , with increasing values with wavelength) to very backscattering ( $-0.178$ , with decreasing values with wavelength) (Fig. 9). Similarly, the 2-term HG function parameters became the most narrowly backscattering of all samples (Fig. 10b). MER Opportunity Pancam data of spherule-rich soils were typically (but not always) backscattering as well. The spherule soils near Vostok crater were modeled with similar 2-term HG phase function parameters as the SCB5 soil with spherules (Fig. 10b).

### 5.4. Apollo soils

The 10084 mare sample exhibits lower  $w$  values than any of the lunar analog samples, while the 68810 highland sample exhibits  $\sim 66\%$  higher  $w$  values, consistent with models of Clementine and other remote sensing observations (Hillier et al., 1999; Kinnelly et al., 2010). The 1-term HG asymmetry parameters were negative (backscattering) for 10084, similar to the bulk JSC-1 sample. Likewise, the 2-term HG modeled  $b$  and  $c$  values (Fig. 11) are more backscattering than any of the lunar analog soils (although close to the results for bulk JSC-1 and FJS-1), and the results from Hillier et al. (1999). These values are similar to the experimental results for agglutinates and clear, rough spheres from McGuire and Hapke (1995). Although  $B0$  values were not well constrained in the mod-

els, average  $h$  values from 1-term HG models were 0.06–0.07, consistent with Clementine model results (Hillier et al., 1999). This is lower than any of the lunar analog soils, and potentially consistent with a more porous nature and/or less uniform grain size distribution than the analog samples. Both Apollo soils exhibit  $\bar{\theta}$  values 14–15°, which is lower than all lunar analogs except FJS-1 and JSC-1AF. For comparison, typical  $\bar{\theta}$  values for lunar regolith surfaces studied by Helfenstein and Shepard (1999) were 24–27°.

The JSC-1A and JSC-1AF samples have the closest similarities to the Apollo soils with respect to  $w$  and  $\bar{\theta}$  values. The JSC-1 analog is more similar in terms of  $h$  values (from 1-term HG models) and  $\xi$  values. The  $b$  and  $c$  parameters from 2-term HG models are only partially matched by the 450 nm and 550 nm results from the JSC-1 and JSC-1A samples, although the FJS-1 values are somewhat similar as well. The magnitude (although not the identical shapes) of phase reddening of the 10084 soil is most like that of the MLS-1 (<1 mm) soil, whereas the curve for the 68810 soil is more similar to the JSC-1AF analog. As such, it is clear that while no lunar soil analogs fully mimic the photometric behaviors of these two Apollo soils, the JSC soil varieties are the most similar overall.

### 5.5. Phase reddening

The variations in near-infrared/visible radiance factor ratios with phase angle (Fig. 14) are certainly influenced by the spectral albedo of the samples. The Mars analog samples are redder in color than the more spectrally neutral SCB5 and lunar analogs, and therefore have more pronounced ratio phase curves. The falloff in ratio values beyond 50–80° phase angles was referred to by Schröder et al. (2011) as an “arch” in their ratio phase curves of laboratory samples. They noted that the arch was not visible for samples dusted with fine powders that formed microstructures on  $\sim 100 \mu\text{m}$  scales, and explained this phenomenon as a geometric optics effect. We note that while none of our samples were dusted, many exhibit the ratio phase curve arch. Adams and Filice (1967) suggested that the reddening resulted from increasing optical path lengths with phase angle (volume scattering) and that the falloff was caused by the transition to surface scattering at large phase angles. Kaydash et al. (2010) similarly stated that the decrease in multiple-scattering (and increasing influence of macroscopic roughness) at large phase angles was the cause for falloffs of ratio phase curves of Apollo soils. Hapke et al. (2012) suggest that the phase reddening observed in LRO WAC data results from a greater contribution from multiple scattering among particles as the wavelength and albedo increase.

For Mercury, Warell and Bergfors (2008) suggest a small phase reddening is observed based on telescopic data, whereas Domingue et al. (2011a) report that no phase reddening is present for Mercury based on MDIS observations. They suggested that phase reddening is due to increased multiple scattering (backscattering) with increasing phase angle, and explained the MDIS data as resulting from Mercury’s observed decrease in backscattering with increasing wavelength.

The MLS-1, FJS-1 samples and the SCB5 soils exhibit the least phase reddening of the samples studied here. However, this is more likely attributable to their spectrally neutral albedo values in the visible/near-infrared (Figs. 5 and 6) than their scattering characteristics, given the variety of scattering types modeled for these samples (Figs. 9–11). The phase reddening exhibited by the Apollo soils (Fig. 15) is consistent with previous work (e.g., Shkuratov et al., 2011), including the color opposition effect near  $10^\circ$  and the crossover between mare and highland soils near  $38^\circ$ . Only the 10084 mare sample shows the increase in ratio values shortward of  $10^\circ$ . This is consistent with the results for Luna soils (Akimov et al., 1979; Shkuratov et al., 2011) where the highland Luna 20 soil exhibited a constant decrease in ratio toward  $0^\circ$  phase angle com-

pared to an increase between 10° and 15° for the Luna 16 and 24 mare samples. However, analysis of the WAC data presented by Hapke et al. (2012) shows the same upturn for at least one of the highlands regions they studied. Additional investigations involving other Apollo soils are warranted to explain the potential disparity between mare and highland soils (e.g., Foote et al., 2012). Similarly, the crossover in 750/450 nm ratios near 38° is consistent with results of Kaydash et al. (2010) for Apollo soils, but the cause for this observation is not clear.

## 6. Conclusions

Our analyses of analog and Apollo soils have revealed a wide range of photometric properties variably related to albedo, color, grain size, and surface texture. To some extent, the type of photometric function used influences the degree to which the Hapke model constrains the model parameters. Not surprisingly, single-scattering albedos ( $w$ ) are the best constrained parameters. The finer-grained samples studied here have high  $w$  values compared to their coarser-grained counterparts, as well as lower macroscopic roughness ( $\bar{\theta}$ ) values. The opposition effect width ( $h$ ) parameter is better constrained by the 1-term HG models. The Mars analog samples exhibit slightly lower  $h$  values (0.06–0.07) than the lunar analogs (~0.07–0.10), whereas the two Apollo soils were modeled with values ~0.05–0.07. The smaller  $h$  values may be consistent with more porous samples with a less uniform grain size distribution. However, Hapke (2008) described how earlier formulations for the shadow-hiding opposition effect were incomplete without accounting for the effects of particle packing. Helfenstein and Shepard (2011) expanded on that work to provide a preliminary, corrected relationship between  $h$  and porosity that improved accuracy of the model for all but very high albedo surfaces. The opposition effect magnitude ( $B_0$ ) is not well constrained by the models, but exhibits values consistently lower than 1.0 for the lunar analog of Apollo soils, potentially suggestive of a lower opacity particles compared to the Mars analog soils.

Comparison of 2-term HG phase function asymmetry parameter ( $b$ ) and backward scattering fraction ( $c$ ) values to the synthetic particles studied by McGuire and Hapke (1995) suggests that the Mars analog soils are typically backscattering and consistent with relatively rough particles with a moderate density of internal scatterers. This is similar to the in situ observations of some soils by the MER Spirit rover. Exceptions are the more forward-scattering, fine-grained SCB5 and JSC-1 (<45  $\mu\text{m}$ ) soils. Some lunar analog soil models result in similar, moderately-forward scattering behaviors (FJS-1, bulk JSC-1 and JSC-1A), as do the two Apollo soils. However, the MLS-1 and JSC-1AF samples populate a narrowly forward-scattering regime (low  $c$ , high  $b$ ) for which no synthetic particles from McGuire and Hapke (1995) provide a good match. Models using MER Pancam data showed that some rover tracks observed by the Opportunity rover and some “gray” rocks by the Spirit rover populate this region of  $b$ ,  $c$  space, as do some glass-rich and/or monocrystalline laboratory samples studied by Souchon et al. (2011). More laboratory analyses are needed to verify and better understand these results.

Model results of the spherule-laden SCB5 soil mimic the model results of soils observed by the MER Opportunity rover relatively well. The addition of spherules caused not only 10–30% albedo darkening, but resulted in the macroscopically roughest surface of all samples studied here ( $\bar{\theta} \sim 26^\circ$ , similar to spherule-rich soils on Mars (Johnson et al., 2006b). This is caused in part by the increase in shadows at higher phase angle. The bimodal grain size distribution may have contributed to the lowest opposition effect width ( $h$ ) value of all samples. The spherules also changed a very forward-scattering soil to a backscattering one, similar to the re-

sults of models from Pancam data acquired near Vostok crater on the Meridiani plains (Johnson et al., 2006b). The addition of spherules also caused phase reddening, an effect observed to variable degrees in all samples, depending on color and albedo. Falloffs in ratio phase curves are also observed in some samples beyond 50–80° phase that are likely related to an increased importance of surface scattering at high angles.

The two Apollo soils were modeled with different Hapke parameters than the lunar analog soils studied here. The closest single-scattering albedo, roughness, opposition effect, and back-scattering matches were from the JSC-1 samples. The phase reddening nature of the 10084 soil was most like MLS-1 bulk soil, although the latter did not exhibit the upturn in ratio values at low phase angles observed for 10084. The lack of this upturn in the 68810 highland sample is an interesting feature matched by analyses of Luna soils (Shkuratov et al., 2011). At this point it remains to be verified whether there is indeed a difference between the highlands and maria, or if this color opposition effect is related to soil maturity state or other physical features. The results presented here are consistent with the concept that most of the phase curve behavior observed in planetary analog soils is due to the micro-scale structure of the surface and not a property of individual particles themselves (e.g., Piatek et al., 2004; Shepard and Helfenstein, 2011). Despite the consistent sample surface preparation techniques used here, the undisturbed microphysical nature of a pristine lunar soil certainly may differ from that of a returned soil observed under laboratory conditions (cf., Velikodsky et al., 2011). The airfall dust-coated (and/or indurated) surfaces of many Mars materials are likewise difficult to replicate at the micro-scale in the lab (cf., Johnson and Grundy, 2001; Johnson et al., 2004). Despite these challenges, continuing work using both laboratory measurements and spacecraft data at many spatial scales will help distinguish the competing influences of spectral albedo, microtopography, composition, compaction, and grain homogeneity on overall scattering behaviors as a function of phase angle. Such information will be vital for interpretations of phase function behavior and material properties from both remote and in situ observations of planetary surfaces.

## Acknowledgments

The authors wish to thank the Planetary Geology and Geophysics program and the Lunar Reconnaissance Orbiter mission for support, and CAPTEM for access to lunar samples. R.V. Morris (JSC), M. Gustafson (Orbitec), P. Bartlett (Honeybee Robotics), and T. White (Penn State) provided samples for this study. Helpful reviews by B. Hapke and P. Helfenstein are appreciated.

## References

- Adams, J.B., Filice, A.L., 1967. Spectral reflectance 0.4 to 20 microns of silicate rock powders. *J. Geophys. Res.* 72, 5705–5715.
- Akimov, L.A., Antipova-Karataeva, I.I., Shkuratov, Y.G., 1979. Indicatrix measurements of lunar samples from landing sites of Luna 24, Luna 16, and Luna 20. *Lunar Planet. Sci.* 10, 9–11.
- Allen, C.C., Graf, J.C., McKay, D.S., 1994. Sintering Bricks on the Moon, Engineering, Construction, and Operations in Space IV. American Society of Civil Engineers, pp. 1220–1229.
- Allen, C.C. et al., 1998. Martian regolith simulant JSC Mars-1. *Lunar Plan. Sci.* XXIX, Abstract #1690.
- Arvidson, R.E. et al., 1989a. Nature and distribution of surficial deposits in Chryse Planitia and vicinity, Mars. *J. Geophys. Res.* 94, 1573–1587.
- Arvidson, R.E., Gooding, J.L., Moore, H.J., 1989b. The martian surface as imaged, sampled, and analyzed by the Viking landers. *Rev. Geophys.* 27, 39–60.
- Beck, P., Pommerol, A., Thomas, N., Schmitt, B., Moynier, F., Barrat, J.-A., 2012. Photometry of meteorites. *Icarus* 218, 364–377. <http://dx.doi.org/10.1016/j.icarus.2011.12.005>.
- Bell III J.F., 1996. Iron, sulfate, carbonate and hydrated minerals on Mars. In: Dyar, M.D., McCammon, C., Schaefer, M.W. (Eds.), *Mineral Spectroscopy: A Tribute to Roger G. Burns*. The Geochemical Society, Special Paper 5.

- Bell III, J.F. et al., 2000. Mineralogic and compositional properties of martian soil and dust: Preliminary results from Mars Pathfinder. *J. Geophys. Res.* 105, 1721–1755.
- Blewett, D.T., Lucey, P.G., Hawke, B.R., Ling, G.G., Robinson, M.S., 1997. A comparison of mercurian reflectance and spectral quantities with those of the Moon. *Icarus* 129, 217–231.
- Buratti, B.J., Hillier, J.K., Wang, M., 1996. The lunar opposition surge: Observations by Clementine. *Icarus* 124, 490–499.
- Capaccioni, F., Ceroni, P., Barucci, M.A., Fulchignoni, M., 1990. Phase curves of meteorites and terrestrial rocks: Laboratory measurements and applications to asteroids. *Icarus* 83, 325–348.
- Clark, B.E., Helfenstein, P., Bell III, J.F., Veverka, J., Izenberg, N., McFadden, L., Wellnitz, D., McFadden, L., 2002. NEAR infrared spectrometer photometry of Asteroid 433 Eros. *Icarus*, 189–204.
- Clark, J.L., McKay, D.S., Taylor, L.A., Carrier III W.D., 2004. Lunar Simulants: JSC-1 is Gone: The Need for New Standardized Root Simulants. Space Resources Roundtable IV (abstract 6023).
- Colwell, J.E., Batiste, S., Horanyi, M., Robertsson, S., Sture, S., 2007. Lunar surface: Dust dynamics and regolith mechanics. *Rev. Geophys.* 45, RG2006. <http://dx.doi.org/10.1029/2005RG000184>.
- Cord, A.M., Pinet, P.C., Daydou, Y., Chevrel, S.D., 2003. Planetary regolith surface analogs: Optimized determination of Hapke parameters using multi-angular spectro-imaging laboratory data. *Icarus* 165, 414–427.
- Domingue, D., Hartman, B., Verbiscer, A., 1997. The scattering properties of natural terrestrial snows versus icy satellite surfaces. *Icarus* 128, 28–48.
- Domingue, D.L., Vilas, F., Holsclaw, G.M., Warrel, J., Izenberg, N.R., Murchie, S.L., Denevi, B.W., Blewett, D.T., McClintock, W.E., Anderson, B.J., Sarantos, M., 2010. Whole-disk spectrophotometric properties of Mercury: Synthesis of MESSENGER and ground-based observations. *Icarus* 209, 101–124.
- Domingue, D.L., Murchie, S.L., Chabot, N.L., Denevi, B.W., Vilas, F., 2011a. Mercury's spectrophotometric properties: Update from the Mercury Dual Imaging System observations during the third MESSENGER flyby. *Planet. Space Sci.* 59, 1853–1872.
- Domingue, D.L. et al., 2011b. Photometric correction of Mercury's global color mosaic. *Planet. Space Sci.* 59, 1873–1887.
- Drief, A., Schiffman, P., 2004. Very low-temperature alteration of sideromelane in hyaloclastites and hyalotuffs from Kilauea and Mauna Kea volcanoes: Implications for the mechanism of palagonite formation. *Clays Clay Miner.* 52 (5), 622–634. <http://dx.doi.org/10.1346/CCMN.2004.0520508>.
- Foote, E.J., Paige, D.A., Johnson, J.R., Grundy, W.M., Shepard, M.T., 2009. The bidirectional reflectance of Apollo 11 soil sample 10084. *Lunar Plan. Sci. XL Abstract 2500*.
- Foote, E.J. et al., 2012. Laboratory and Diviner Bidirectional reflectance measurements of Apollo soils. *Lunar Planet. Sci.* 43, Abstract #2357.
- Gehrels, T., Coffeen, T., Owings, D., 1964. Wavelength dependence of polarization. III. The lunar surface. *Astron. J.* 69, 826–852.
- Goguen, J.D., Stone, T.C., Kieffer, H.H., Buratti, B.J., 2010. A new look at photometry of the Moon. *Icarus* 208, 548–557.
- Goldich, S.S., 1970. Lunar and terrestrial ilmenite basalt. *Science* 171 (3977), 1245–1246.
- Gradie, J.C., Veverka, J., Buratti, B.J., 1980. The effects of photometric geometry on spectral reflectance. *Proc. Lunar Sci. Conf.* 11, 357–359.
- Guinness, E.A., Arvidson, R.E., Clark, I.H.D., Shepard, M.K., 1997. Optical scattering properties of terrestrial varnished basalts compared with rocks and soils at the Viking Lander sites. *J. Geophys. Res.* 102, 28687–28703.
- Gunderson, K., Thomas, N., 2008. Polarimetric NIR reflectance measurements of regolith simulants at zero phase angle. *Planet. Space Sci.* 56, 1925–1938.
- Gunderson, K., Thomas, N., Whitty, J., 2006. First measurements with the Physikalisches Institut Radiometric Experiments (PHIRE). *Planet. Space Sci.* 54, 1046–1056.
- Hamilton, V.E., Morris, R.V., Gruener, J.E., Mertzman, S.A., 2008. Visible, near-infrared, and middle infrared spectroscopy of altered basaltic tephra: Spectral signatures of phyllosilicates, sulfates, and other aqueous alteration products with application to the mineralogy of the Columbia Hills of Gusev Crater, Mars. *J. Geophys. Res.*, 113. <http://dx.doi.org/10.1029/2007JE003049>.
- Hapke, B., 1993. *Theory of Reflectance and Emittance Spectroscopy*. Cambridge University Press, 455 pp.
- Hapke, B., 2002. Bidirectional reflectance spectroscopy. V. The coherent backscatter opposition effect and anisotropic scattering. *Icarus* 157, 523–534.
- Hapke, B., 2008. Bidirectional reflectance spectroscopy. VI. Effects of porosity. *Icarus* 195, 918–926.
- Hapke, B., 2012. *Theory of Reflectance and Emittance Spectroscopy*, second ed. Cambridge University Press, 520 pp.
- Hapke, B., Kopal, Z. (Eds.), 1971. *Physics and Astronomy of the Moon*, second ed. Academic Press, New York, p. 155.
- Hapke, B.W., Nelson, R.M., Smythe, W.D., 1993. The opposition effect of the Moon: The contribution of coherent backscatter. *Science* 260, 509–511.
- Hapke, B.W., Nelson, R., Smythe, W., 1998. The opposition effect of the Moon: Coherent backscatter and shadow hiding. *Icarus* 133, 89–97.
- Hapke, B.W., Shepard, M.K., Nelson, R.M., Smythe, W.D., Piatek, J.L., 2009. A quantitative test of the ability of models based on the equation of radiative transfer to predict the bidirectional reflectance of a well-characterized medium. *Icarus* 199, 210–218.
- Hapke, B.W., Denevi, B., Sato, H., Braden, S., Robinson, M., 2012. The wavelength dependence of the lunar phase curve as seen by the Lunar Reconnaissance Orbiter wide-angle camera. *J. Geophys. Res.* 117, E00H15. <http://dx.doi.org/10.1029/2011JE003916>.
- Hartman, B., Domingue, D., 1998. Scattering of light by individual particles and the implications for models of planetary surfaces. *Icarus* 131, 421–448.
- Helfenstein, P., Veverka, J., 1987. Photometric properties of lunar terrains derived from Hapke's equation. *Icarus* 72, 342–357.
- Helfenstein, P., Shepard, M., 1999. Submillimeter-scale topography of the lunar regolith. *Icarus* 141, 107–131.
- Helfenstein, P., Shepard, M., 2007. A blind test of Hapke's photometric model. *J. Geophys. Res.* 112, E03001. <http://dx.doi.org/10.1029/2005JE002625>.
- Helfenstein, P., Shepard, M., 2011. Testing the Hapke photometric model: Improved inversion and the porosity correction. *Icarus* 215, 83–100.
- Hillier, J.K., Buratti, B.J., Hill, K., 1999. Multispectral photometry of the Moon and absolute calibration of the Clementine UV/VIS camera. *Icarus* 141, 205–225.
- Jehl, A., Pinet, P., Baratoux, D., Daydou, Y., Chevrel, S., Heuripeau, F., Manaud, N., Cord, A., Rosemberg, C., Neukum, G., Gwinner, K., Scholten, F., Hoffman, H., Roatsch, T., 2008. The HRSC Team, Gusev photometric variability as seen from orbit by HRSC/Mars-express. *Icarus* 197, 403–428. <http://dx.doi.org/10.1016/j.icarus.2008.05.022>.
- Johnson, J.R., Grundy, W.M., 2001. Visible/near-infrared spectra and two-layer modeling of palagonite-coated basalts. *Geophys. Res. Lett.* 28, 2101–2104.
- Johnson, J.R. et al., 1999. Preliminary results on photometric properties of materials at the Sagan Memorial Station Mars. *J. Geophys. Res.* 104, 8809–8830.
- Johnson, J.R., Christensen, P.R., Lucey, P.G., 2002. Dust coatings on basaltic rocks and implications for thermal infrared spectroscopy of Mars. *J. Geophys. Res.* 107(E6). <http://dx.doi.org/10.1029/2000JE001405>.
- Johnson, J.R., Grundy, W.M., Shepard, M.K., 2004. Visible/near-infrared spectrogoniometric observations and modeling of dust-coated rocks. *Icarus* 171, 546–556.
- Johnson, J.R. et al., 2006a. Radiative transfer modeling of dust-coated Pancam calibration target materials: Laboratory visible/near-infrared spectrogoniometry. *J. Geophys. Res.* 111, E12507. <http://dx.doi.org/10.1029/2005JE002658>.
- Johnson, J.R. et al., 2006b. Spectrophotometric properties of materials observed by Pancam on the Mars Exploration Rovers: 1. Spirit. *J. Geophys. Res.* 111, E02514. <http://dx.doi.org/10.1029/2005JE002494>.
- Johnson, J.R. et al., 2006c. Spectrophotometric properties of materials observed by Pancam on the Mars Exploration Rovers: 2. Opportunity. *J. Geophys. Res.* 111, E12516. <http://dx.doi.org/10.1029/2006JE002762>.
- Johnson, J.R., Shepard, M.K., Grundy, W., Morris, R.M., White, T.S., 2008. Spectrogoniometric measurements and models of lunar analog soils. *Lunar Planet. Sci. XXXIX Abstract 1331*.
- Johnson, J.R. et al., 2008. Physical properties of the martian surface from spectrophotometric observations. In: *The Martian Surface: Composition Mineralogy, and Physical Properties*. Cambridge University Press, pp. 428–450 (Chapter 19).
- Kaasalainen, S., 2003. Laboratory photometry of planetary regolith analogs: I. Effects of grain and packing properties on opposition effect. *Astron. Astrophys.* 409, 765–769.
- Kamei, A., Nakamura, A.M., 2002. Laboratory study of the bidirectional reflectance of powdered surfaces: On the asymmetry parameter of asteroid photometric data. *Icarus* 156, 551–561.
- Kanamori, H., Udagawa, S., Yoshida, T., Matsumoto, S., Takagi, K., 1998. Properties of lunar soil simulant manufactured in Japan, in Space 98. In: Galloway, R.G., Lokaj, Stanley (Eds.), *Proceedings of the Sixth International Conference and Exposition on Engineering, Construction and Operations in Space*, p. 462.
- Kawakami, K., Nakamura, A.M., 2007. Near infrared opposition surge of carbonaceous chondrite meteorites. *Lunar Planet. Sci. XXXVIII Abstract #1531*.
- Kaydash, V.G. et al., 2010. The phase ratios of the color index: Mapping of two regions of the near side of the Moon. *Solar Syst. Res.* 44, 267–280.
- Kennelly, E.J., Price, S.D., Kraemer, K.E., Aschbrenner, R., 2010. Calibration against the Moon I: A disk-resolved lunar model for absolute reflectance calibration. *Icarus* 210, 14–36.
- Kieffer, H.H., Stone, T.C., 2005. The spectral irradiance of the Moon. *Astron. J.* 129, 2887–2901.
- Magrin, S. et al., 2012. The OSIRIS team, (21) Lutetia spectrophotometry from Rosetta-OSIRIS images and comparison to ground-based observations. *Planet. Space Sci.* 66, 43–53.
- Marquardt, D.W., 1963. An algorithm for least-squares estimation of nonlinear parameters. *J. Soc. Ind. Appl. Math.* 11, 431–441.
- McGuire, A.F., Hapke, B.W., 1995. An experimental study of light scattering by large, irregular particles. *Icarus* 113, 134–155.
- McKay, D.S., Carter, J.L., Boles, W.W., Allen, C.C., Allton, J.H., 1994. JSC-1: A New Lunar Soil Simulant, Engineering, Construction, and Operations in Space IV. American Society of Civil Engineers.
- Morris, R.V. et al., 2000. Mineralogy, composition, and alteration of Mars Pathfinder rocks and soils: Evidence from multispectral, elemental, and magnetic data on terrestrial analogue, SNC meteorite, and Pathfinder samples. *J. Geophys. Res.* 105, 1757–1817.
- Morris, R.V. et al., 2001. Phyllosilicate-poor palagonitic dust from Mauna Kea Volcano (Hawaii): A mineralogical analogue for magnetic martian dust? *J. Geophys. Res.* 106, 5057–5083.
- Mustard, J.F., Pieters, C.M., 1989. Photometric phase functions of common geologic minerals and applications to quantitative analysis of mineral mixture reflectance spectra. *J. Geophys. Res.* 94, 13619–13634.

- Näränen, J., Kaasalainen, S., Peltoniemi, J., Heikkilä, S., Granvik, M., Saarinen, V., 2004. Laboratory photometry of planetary regolith analogs: II. Surface roughness and extremes of packing density. *Astron. Astrophys.* 426, 1103–1109.
- NASA-MSFC, 2006. Characterization Summary of JSC-1AF Lunar Mare Regolith Simulant, 1.6.2 ed. NASA Marshall Space Flight Center.
- Nelder, J., Mead, R., 1965. A simplex method for function minimization. *Comput. J.* 7, 308–313.
- Nelson, R.M., Hapke, B.W., Smythe, W.D., Horn, L.J., 1998. Phase curves of selected particulate materials: The contribution of coherent backscattering to the opposition surge. *Icarus* 131, 223–230.
- O'Leary, B., Briggs, F., 1970. Optical properties of Apollo 11 Moon samples. *J. Geophys. Res.* 75, 6532–6538.
- Piatek, J.L., Hapke, B.W., Nelson, R.M., Smythe, W.D., Hale, A.S., 2004. Scattering properties of planetary regolith analogs. *Icarus*, 531–545.
- Pieters, C.M., Pratt, S., Hoffmann, H., et al., 1991. Bidirectional spectroscopy of returned lunar soils: Detailed "ground truth" for planetary remote sensors. *Lunar Planet. Sci. XXII*, 1069–1070.
- Pinet, P.C. et al., 2005. Mars express imaging photometry and surface geologic processes at Mars: What can be monitored within Gusev crater? *Lunar Planet. Sci. XXXVI*. Abstract 1721.
- Press, William H. et al., 1992. *Numerical Recipes in C: The Art of Scientific Computing*. Cambridge University Press, Cambridge.
- Rosenbush, V.K., Shevchenkob, Vasilij G., Kiseleva, Nikolai N., Sergeevc, Alexander V., Shakhovskoyd, Nikolai M., Velichkob, Feodor P., Kolesnikove, Sergey V., Karpovc, Nikolai V., 2009. Polarization and brightness opposition effects for the E-type Asteroid 44 Nysa. *Icarus* 201, 655–665.
- Sanchez, J.A., Reddy, V., Nathues, A., Cloutis, E.A., Mann, P., Hiesinger, H., 2012. Phase reddening on near-Earth asteroids: Implications for mineralogical analysis, space weathering and taxonomic classification. *Icarus* 220, 36–50.
- Schiffman, P., Southard, R.J., Eberl, D.D., Bishop, J.L., 2002. Distinguishing palagonitized from pedogenetically altered basaltic Hawaiian tephra: Mineralogical and geochemical criteria. In: Smellie, J.L., Chapman, M. (Eds.), *Volcano–Ice Interaction on Earth and Mars*. *Geol. Soc. London*, vol. 202, pp. 393–405.
- Schröder, S.E., Gynko, Y., Pommerol, A., Keller, H.U., 2011. Phase Reddening Observed in the Laboratory. EPSC-DPS Joint Meeting, vol. 6, EPSC-DPS011-1841.
- Seiferlin, K., Ehrenfreund, P., Garry, J., Gunderson, K., Hütter, E., Kargl, G., Maturilli, A., Merrison, J.P., 2008. Simulating Martian regolith in the laboratory. *Planetary and Space Science* 56, 2009–2025. <http://dx.doi.org/10.1016/j.pss.2008.09.01>.
- Shaw, A., Arvidson, R.E., Wolff, M.J., Seelos, F.P., Wiseman, S.M., Cull, S., 2012. Determining surface roughness and additional terrain properties: using opportunity Mars rover results to interpret orbital data for extended mapping. In: *Proceedings of the forty third Lunar and Planetary Science Conference*, No. 1659, ID 1644.
- Shepard, M.K., 2001. The Bloomsburg University Goniometer (B.U.G.) laboratory: An integrated laboratory for measuring bidirectional reflectance functions. *Lunar Planet. Sci. XXXII*. Abstract #1015.
- Shepard, M.K., Helfenstein, P., 2007. A test of the Hapke photometric model. *J. Geophys. Res.* 112, E03001. <http://dx.doi.org/10.1029/2005JE002625>.
- Shepard, M.K., Helfenstein, P., 2011. A laboratory study of the bidirectional reflectance from particular samples. *Icarus* 215, 526–533.
- Shevchenko, V.V., Pinet, P., Chevrel, S., Pugacheva, S.G., Daydou, Y., 2003. Lunar photometry and composition of ejecta terrains with AMIE/SMART-1. *Lunar Planet. Sci. XXXIV*. Abstract 1113.
- Shkuratov, Y., Kreslavsky, M.A., Ovcharenko, A.A., Stankevich, D.G., Zubko, E.S., 1999. Opposition effect from Clementine data and mechanisms of backscatter. *Icarus* 141, 155–231.
- Shkuratov, Y., Bondarenko, S., Kadash, V., Videen, G., Munoz, O., Volten, H., 2007. Photometry and polarimetry of particulate surfaces and aerosol particles over a wide range of phase angles. *J. Quant. Spectrosc. Radiat. Trans.* 106, 487–508.
- Shkuratov, Y., Kaydash, V., Korokhin, V., Velikodsky, Y., Opanasenko, N., Videen, G., 2011. Optical measurements of the Moon as a tool to study its surface. *Planet. Space Sci.* 59, 1326–1371.
- Souchon, A.L., Pinet, P.C., Chevrel, S.D., Daydou, Y.H., Baratoux, D., Kurita, K., Shepard, M.K., Helfenstein, P., 2011. An experimental study of Hapke's modeling of natural granular surface samples. *Icarus* 215, 313–331.
- Taylor, L.A., Pieters, C.M., Keller, L.P., Morris, R.V., McKay, D.S., 2001. Lunar Mare Soils: Space weathering and the major effects of surface-correlated nanophase Fe. *J. Geophys. Res.* 106, 27985–27999. <http://dx.doi.org/10.1029/2000JE001402>.
- Velikodsky, Y.I., Opanasenko, N.V., Akimov, L.A., Korokhin, V.V., Shkuratov, Yu.G., Kaydash, V.G., Videen, G., Ehgamberdiev, Sh.A., Berdalieva, N.E., 2011. New Earth-based absolute photometry of the Moon. *Icarus* 214, 30–45.
- Warell, J., Bergfors, C., 2008. Mercury's integral phase curve: Phase reddening and wavelength dependence of photometric quantities. *Planet. Space Sci.* 56 (15), 1939–1948.
- Weiblen, P.W., Gordon, K., 1988. Characteristics of a Simulant for Lunar Surface Materials. *LPI Contrib.* 652, 254.
- Weiblen, P.W., Murawa, M.J., Reid, K.J., 1990. Preparation of simulants for lunar surface materials. *Engineering, Construction, and Operations in Space II*, vol. 1. American Society of Civil Engineers, New York, p. 98.
- White, T. et al., 2000. The Paleoclimatological Significance of Albian Sphaerosiderites from Eastern Saskatchewan and Western Manitoba. *Sk. Geol. Surv., Sk. Energy & Mines, Summ. Inv.* 2000-4.1, pp. 63–75.
- White, T., Ludvigson, G., Gonzalez, L., Poulsen, C., 2001. The mid-Cretaceous Greenhouse Hydrologic Cycle of North America. *Geology* 29 (4), 363–366.
- Yokota, Y. et al., 2011. Lunar photometric properties at wavelengths 0.5–1.6  $\mu\text{m}$  acquired by SELENE Spectral Profiler and their dependency on local albedo and latitudinal zones. *Icarus* 215, 639–660.